The Astrophysical Journal, 1000:92 (21pp), 2026 March 20 https://doi.org/10.3847/1538-4357/ae40ad

On the Contradictory Case of the Binary System HD 81809 Hosting Two Pulsating Solar-like Stars Observed by TESS

Maria Pia Di Mauro[1], Camilla Pezzotti[2], Nuno Moedas[1], Giovanni Catanzaro[3], Pierre F. L. Maxted[4], Enrico Corsaro[3], Raffaele Reda[5], Richard Scuflaire[2], Alfio Maurizio Bonanno[3], Luca Giovannelli[5], and Paul G. Beck[6]
[1] INAF-IAPS, Via del Fosso del Cavaliere 100, Roma, Italy; maria.dimauro@inaf.it
[2] STAR Institute, Université de Liège, Liège, Belgium
[3] INAF-Osservatorio Astrofisico di Catania, Via S. Sofia 81, Catania, Italy
[4] Astrophysics Group, Keele University, Keele, Staffordshire ST5 5BG, UK
[5] Dipartimento di Fisica, Università di Roma Tor Vergata, Roma, Italy
[6] Universidad de La Laguna, Santa Cruz de Tenerife, Santa Cruz de Tenerife, Spain
Received 2025 July 2; revised 2026 January 12; accepted 2026 January 23; published 2026 March 16

Abstract

We present a new comprehensive study of HD 81809, a nearby binary system of two solar-like stars showing high-amplitude X-ray emission and a well-defined 8 yr solar-like magnetic cycle. By analyzing high-resolution spectroscopy, alongside Gaia Data Release 3 (DR3) astrometry and bolometric fluxes, we derive updated fundamental parameters for both components. In particular, we uncover a significant chemical difference: the primary is metal poor ([Fe/H] $\simeq -0.57$), while the secondary shows solar-like metallicity ([Fe/H] $\simeq 0.00$). This suggests that the system originated in a mildly metal-poor environment, consistent with the Galactic thick disk population, and that the secondary's surface composition has been altered by a recent accretion event. Using multisector TESS photometry, we detected solar-like oscillations in both components, deriving global asteroseismic parameters $\Delta\nu = 43.32 \pm 3.91$ μHz and $\nu_{\rm max} = 708.74^{+3.23}_{-3.74}$ μHz for HD 81809 A, and $\Delta\nu = 97.75 \pm 4.49$ μHz and $\nu_{\rm max} = 2098.07^{+3.07}_{-2.83}$ μ Hz for HD 81809 B. By combining all the observational constraints with stellar evolutionary models computed using the CLES and MESA codes, we reconstructed the evolutionary scenario of the system. Our results indicate that HD 81809 is an old system with an age of $\sim$10 Gyr, composed of a subgiant primary with mass $M \sim 0.87$ $_{\odot}$ and radius $R \sim 1.96\,R_{\odot}$—likely responsible for the reactivated dynamo cycle—and a main-sequence secondary with mass $M \sim 0.85\,M_{\odot}$ and radius $R \sim R\,1.10\,R_{\odot}$. This system represents a benchmark for studying stellar evolution, magnetic activity, and the physics of old, metal-poor stars in the Galactic thick disk.

Unified Astronomy Thesaurus concepts: A stars (5); B subgiant stars (125); Asteroseismology (73); High resolution spectroscopy (2096); Solar cycle (1487); Galactic archaeology (2178); Stellar evolutionary models (2046); Binary stars (154)

1. Introduction

The system HD 81809 (HIP 46404, TIC 46802551, HR 3750) is a close visual binary characterized by a maximum separation $\rho = 0\farcs487$, an orbit with a semimajor axis of $\alpha = (0\farcs428 \pm 0\farcs001)$, an orbital period of $P = 34.8 \pm 0.06$ yr, and an inclination $i_{\rm orb} = 85\fdg4 \pm 0\fdg$, as obtained from SOAR speckle photometry by A. Tokovinin et al. (2015). The distance according to the C. A. L. Bailer-Jones et al. (2021) catalog is $d = (30.907 \pm 0.335)$ pc, as estimated from the Gaia Data Release 3 (DR3) parallax $\pi = (32.29 \pm 0.36)$ mas.

The two components show apparent magnitudes of $V_{\rm A} = 5.56 \pm 0.01$ and $V_{\rm B} = 7.45 \pm 0.01$, respectively (R. Egeland 2018). The primary HD 81809 A (HR 3750, TIC 46802551) is a G1.5 solar-type star with $T_{\rm eff,A} = (5757 \pm 57)$ K from two-color photometry (R. Egeland 2018), and $T_{\rm eff,A} = (5620 \pm 80)$ K from high-resolution spectroscopy (K. Fuhrmann & R. Chini 2018). Its rotational period is $P_{\rm rot,A} = (40.2 \pm 2.3)$ days as derived by R. A. Donahue (1993), R. A. Donahue et al. (1996), and R. Egeland (2018). The secondary seems to be a G-type star too, with $T_{\rm eff,B} = (5705 \pm 73)$ K as obtained from two-color photometry (R. Egeland 2018), quite in agreement with $T_{\rm eff,B} = (5730 \pm 100)$ K deduced from high-resolution spectroscopy by K. Fuhrmann & R. Chini (2018).

Binary stars in which one or both components can be detected asteroseismically provide powerful constraints on our understanding of stellar physics. The HD 81809 system appears particularly interesting, because it has been observed with different instruments at different epochs, which allowed astronomers to collect several pieces of information. Among these, it should be mentioned a well-defined magnetic activity cycle similar to that of the Sun with a period $\simeq 8.2$ yr (R. Egeland 2018) detected through the regular modulation of chromospheric indicators.

The system is also characterized by high-amplitude and cyclically emitted X-ray flux, as monitored by the XMM-Newton program, which seems to originate from the more massive of the two components (F. Favata et al. 2004, 2008; S. Orlando et al. 2017).

Even though this object has been largely observed, the question of the characterization of the two components is still quite debated and the estimate of the ages and masses appears to be quite crucial. In particular considering that the age of a star is one of the most challenging parameters to determine because it is usually inferred through indirect methods (Y. Lebreton et al. 2014). In this regard, by using stellar evolutionary models, K. Fuhrmann & R. Chini (2018)

estimated for the primary component a value of age $\tau = 3.2$ Gyr for a mass $M_A = (1.39 \pm 0.09)\, M_\odot$ in contradiction with the long rotational period resulted by the action of magnetic braking and the estimated low spectroscopic iron-to-magnesium abundance $[Fe/Mg] = -0.35 \pm 0.05$, which classifies this target as a Population II star (thick disk). In order to reconcile this contradictory scenario, K. Fuhrmann & R. Chini (2018) hypothesized that the young massive primary subgiant could be the result of a fossil merger between an old progenitor with mass $\simeq 1.0\, M_\odot$ and a former tertiary component with a mass of $\simeq 0.39\, M_\odot$.

The purpose of this manuscript is to draw new conclusions on the fundamental parameters of HD 81809, taking advantage of the photometric time series and asteroseismic measurements provided by the TESS (G. R. Ricker et al. 2014) space mission, which, combined with the spectroscopic atmospheric results, allow us to define a new evolutionary scenario, confirmed by all the available observational data.

The manuscript is organized as follows: In Section 2 we will present the revised orbital parameters, masses, luminosities, and a new analysis of HERMES high-resolution spectra to obtain a complete set of atmospheric parameters and the elemental abundances for the two stars. In Section 3 an analysis of the TESS photometric light curve will be presented in order to extract the global oscillation parameters. In Section 4 we will characterize the properties of the two stars of HD 81809 based on the spectroscopic atmospheric parameters and the TESS asteroseismic data, supplemented by stellar masses and luminosities. In Section 5 we will present an analysis of the magnetic activity measurements to confirm the evolutionary stage. In Section 6 we will present a rotational evolutionary model of the primary component and compare it with the observed X-ray flux. In Section 7 we will make our considerations and conclusion.

2. Fundamental Parameters of HD 81809

2.1. Radial Velocity Measurements

We analyzed high-resolution spectroscopic observations of HD 81809 obtained with several instruments spanning more than two decades. The largest and most precise contribution comes from 12 spectra acquired between 2012 January 10 and 2013 January 18 with the HERMES spectrograph on the MERCATOR 1.2 m telescope, retrieved from the Mercator library of stellar spectroscopy (P. Royer et al. 2024). HERMES operates at a resolving power of $R \approx 85{,}000$. The cross-correlation functions (CCFs), computed using a numerical mask based on the solar spectrum, exhibit two well-separated peaks corresponding to the two stellar components (Figure 1).

RVs were extracted by performing a simultaneous least-squares fit of two Gaussian profiles to each CCF. The mean FWHM of the best-fit Gaussian profiles are 8.15 ± 0.01 km s^{-1} for HD 81809 A and 7.26 ± 0.09 km s^{-1} for HD 81809 B.

We complemented the HERMES dataset with several archival observations. A spectrum obtained on 1996 December 01 with the HIRES spectrograph on the Keck I telescope (nominal resolving power $R \approx 71{,}700$) was retrieved from the Keck Observatory Archive. The CCF for this spectrum appeared clearly asymmetric, so we also performed a least-squares fit of two Gaussian functions to measure the RVs of both stars with the FWHM of the two Gaussian profiles set equal to one another.

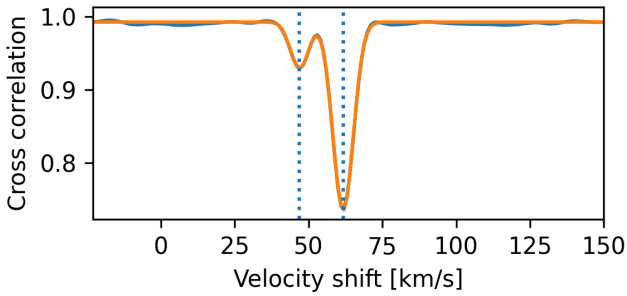

Figure 1. A CCF for one HERMES spectrum of HD 81809 with the double-Gaussian fit used to measure the radial velocities (RVs) of the two stars.

Two spectra of HD 81809 observed on the night 1998 January 14 with the 1.93 m telescope of Observatoire de Haute Provence with the ELODIE spectrograph were retrieved from the ELODIE data archive. These spectra have a nominal resolving power of $R \approx 42{,}000$. These spectra also produced asymmetric CCFs and so we fit them in the same way as we did for the HIRES spectra.

Finally, two spectra observed on 2017 May 09 and 2018 January 12 with the FEROS spectrograph mounted on the ESO/MPG 2.3 m telescope at La Silla (A. Kaufer et al. 1999) were included. These spectra, with resolving power $R \approx 48{,}000$, display symmetric CCFs and were therefore fitted with a single-Gaussian profile to derive RVs for the primary component only. All RV measurements and residuals from the best-fit orbit are reported in Table 1.

2.2. Orbital Solution and Stellar Masses

The orbital solution was obtained by fitting a Keplerian model simultaneously to the RVs and to measurements of the relative astrometric positions of the two stars. In addition to our new RV measurements, we included published velocities from the Ninth Catalogue of Spectroscopic Binary Orbits (SB9; D. Pourbaix et al. 2004). The astrometric dataset consists of angular separations and position angles compiled from the literature (see Appendix Table A1).

The posterior probability distributions of the orbital parameters were sampled using the affine-invariant Markov Chain Monte Carlo (MCMC) ensemble sampler implemented in the EMCEE package (D. Foreman-Mackey et al. 2013). We assumed Gaussian uncertainties for all observables and adopted broad, uniform priors on all model parameters. Position angles obtained from speckle interferometry suffer from a 180° ambiguity, which we resolved by comparing their temporal evolution with the astrometric orbit published by R. Egeland (2018).

The orbital parameters derived from our analysis are listed in Table 2. Correlations among selected parameters are presented in Figure 2, while the best-fit model is overplotted on the RV and astrometric data in Figure 3. The orbital parallax derived from the joint solution, $\pi = 32.3 \pm 0.8$ mas, is in excellent agreement with the Gaia DR3 value of $\pi = 32.3 \pm 0.4$ mas.

The masses of HD 81809 A and HD 81809 B were determined through a joint analysis of the RV measurements and relative astrometry. We performed a simultaneous fit of a Keplerian orbit to the spectroscopic and visual data, allowing us to derive a fully constrained orbital solution. The resulting

Table 1
Radial Velocity Measurements for HD 81809 A and HD 81809 B and the Residuals from the Best-fit Orbit

MJD	$V_{r,A}$ (km s^{-1})	$(O-C)_A$ (km s^{-1})	$V_{r,B}$ (km s^{-1})	$(O-C)_B$ (km s^{-1})	Phase	Source
21615.0	54.65	+0.68	⋯	⋯	0.348	SB9
22338.4	51.50	−1.38	⋯	⋯	0.405	SB9
22631.0	52.67	+0.13	⋯	⋯	0.428	SB9
24192.0	52.70	+1.05	⋯	⋯	0.552	SB9
39907.0	54.23	−1.18	⋯	⋯	0.801	SB9
40780.0	56.89	−0.98	⋯	⋯	0.870	SB9
41338.0	58.28	−1.34	⋯	⋯	0.915	SB9
43510.0	60.71	−0.80	47.14	−0.18	0.087	SB9
45269.0	57.24	+0.02	51.42	−1.11	0.227	SB9
45911.0	55.53	−0.18	56.51	+2.15	0.278	SB9
46635.0	54.00	−0.25	59.65	+3.52	0.335	SB9
55964.1	61.81	+0.06	47.09	+0.06	0.076	HERMES
55976.1	61.77	+0.04	47.10	+0.05	0.077	HERMES
55938.2	61.82	+0.03	47.01	+0.03	0.074	HERMES
55998.0	61.61	−0.08	47.01	−0.09	0.079	HERMES
56310.1	61.11	+0.03	47.85	+0.02	0.104	HERMES
56062.9	61.53	−0.04	47.14	−0.10	0.084	HERMES
55938.2	61.82	+0.04	47.02	+0.04	0.074	HERMES
55983.0	61.70	−0.01	47.03	−0.03	0.078	HERMES
55976.1	61.76	+0.03	47.09	+0.03	0.077	HERMES
55937.1	61.74	−0.05	46.93	−0.04	0.074	HERMES
56310.1	61.10	+0.02	47.86	+0.03	0.104	HERMES
55983.0	61.70	−0.01	47.05	−0.02	0.078	HERMES
50418.6	50.49	−1.54	60.19	+1.35	0.636	HIRES
50828.1	51.45	−0.97	60.24	+1.87	0.668	ELODIE
50828.6	51.46	−0.96	60.28	+1.91	0.668	ELODIE
57858.5	56.20	−1.01	⋯	⋯	0.227	FEROS
58091.9	56.15	−0.50	⋯	⋯	0.245	FEROS

Table 2
Orbital Parameters of the Combined Spectroscopic and Astrometric Solution for HD 81809

Parameter	Value	Units	Notes
T	2455083 ± 211	JD	Time of periastron
P	34.53 ± 0.16	yr	Orbital period
K_A	5.42 ± 0.17	km s^{-1}	Semiamplitude of the primary spectroscopic orbit
K_B	6.30 ± 0.25	km s^{-1}	Semiamplitude of the secondary spectroscopic orbit
γ	54.93 ± 0.21	km s^{-1}	RV of system barycenter
α	0.4089 ± 0.0079	″	Semimajor axis of the visual orbit
e	0.366 ± 0.022	⋯	Orbital eccentricity
ω	347.5 ± 6.7	°	Longitude of periastron for the primary star orbit
Ω	150.42 ± 0.39	°	Longitude of ascending node
$\sin i$	0.9968 ± 0.0005	⋯	sin(orbital inclination)
σ_A	0.94 ± 0.21	km s^{-1}	Standard error on the primary star RVs excluding HERMES
σ_B	2.38 ± 0.77	km s^{-1}	Standard error on the secondary star RVs excluding HERMES
$\sigma_{A,H}$	0.049 ± 0.012	km s^{-1}	Standard error on the HERMES primary star RVs
$\sigma_{B,H}$	0.061 ± 0.015	km s^{-1}	Standard error on the HERMES secondary star RVs
$\sigma_{\rho,S}$	0.0361 ± 0.0054	″	Standard error on the speckle ρ measurements
$\sigma_{\rho,M}$	0.080 ± 0.017	″	Standard error on the micrometer ρ measurements
$\sigma_{\theta,S}$	2.25 ± 0.38	°	Standard error on the speckle PA measurements
$\sigma_{\theta,M}$	3.57 ± 0.72	°	Standard error on the micrometer PA measurements

Note. The fit uses the measured RVs of both components together with their relative astrometric positions. Angles follow the standard visual-orbit convention: ω refers to the primary star, and Ω is the position angle of the ascending node. T is given as the JD (barycentric dynamical time) time of periastron passage. Quoted σ values represent additional Gaussian error terms fitted for each dataset.

mass estimates represent a significant improvement over previous determinations, primarily due to the inclusion of high-resolution spectra that clearly resolve both components of this SB2 system and provide RVs for each star. The stellar masses inferred are reported in Table 3.

2.3. Atmospheric Parameters from Spectroscopic Analysis

We determined the overall iron abundance and derived detailed abundances for several other chemical elements from a high-resolution HERMES spectrum obtained by averaging nine individual spectra, all taken near orbital quadrature

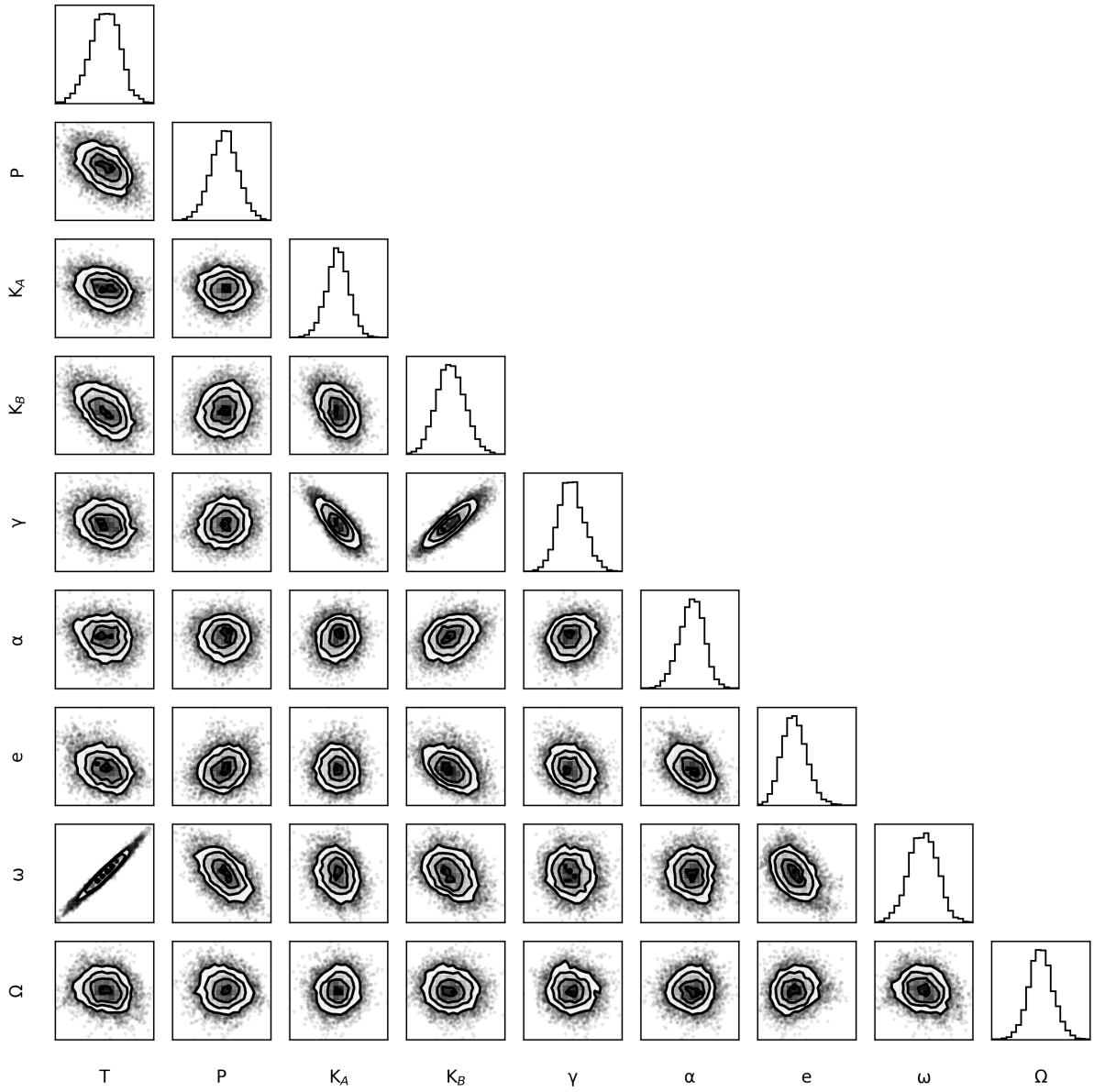

Figure 2. Correlation plot for the parameters of interest given in Table 2 derived from the fit of the visual and spectroscopic orbits to RV, position angle, and angular separation measurements for HD 81909.

(phases between 0.074 and 0.079, see Table 1) to maximize the separation between the components and enhance the visibility of lines from both the primary and the secondary, achieving a signal-to-noise ratio of ∼500 at $\lambda = 6000$ Å, thus providing a comprehensive picture of the stellar chemical composition.

The determination of chemical abundances began with the definition of the primary atmospheric parameters: effective temperature ($T_{\rm eff}$), surface gravity ($\log g$), microturbulent velocity (ξ), and projected rotational velocity ($v \sin i$).

To estimate the effective temperature, we applied to both components the line depth ratio (LDR) method (V. V. Kovtyukh & N. I. Gorlova 2000), which is sensitive to temperature variations and is largely unaffected by abundance differences or interstellar reddening. For our spectrum, we measured approximately 32 LDRs using the calibration lines listed in V. V. Kovtyukh & N. I. Gorlova (2000). The final temperature and its uncertainty were derived as the mean value and the weighted standard deviation of these measurements.

The remaining parameters (ξ and $\log g$) were derived through an iterative process. The microturbulent velocity was obtained by requiring the iron abundance to be independent of line strength, i.e., ensuring a null slope in the [Fe/H] versus equivalent width (EW) diagram. We measured the EWs of 145 Fe I lines using a custom semiautomatic routine written in IDL, with line data taken from M. Romaniello et al. (2008). These EWs were converted into abundances using the WIDTH9 code (R. L. Kurucz & E. H. Avrett 1981), in combination with model atmospheres computed with ATLAS9 (R. L. Kurucz 1993). Since Fe I lines are insensitive to surface gravity, $\log g$ was determined by imposing ionization equilibrium between Fe I and Fe II, using 24 Fe II lines from the same reference. Errors were estimated by propagating the uncertainties from the linear fits.

The final atmospheric parameters, adopted for the two components, are reported in Table 3. The values result in good agreement, within the errors, with previous measurements.

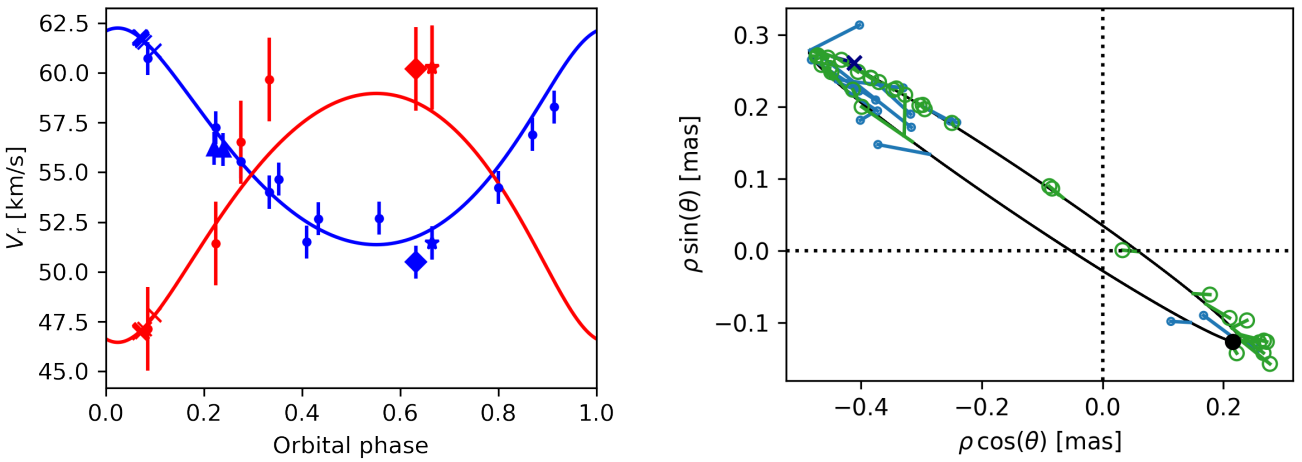

Figure 3. Left panel: RV measurements for HD 81809 A (blue points) and HD 81809 B (red points) with the best-fit spectroscopic orbit (solid lines). Symbols denote the source of the RV measurements as follows: crosses—HERMES; diamonds—HIRES; triangles—FEROS; stars—ELODIE; and dots—SB9. Right panel: measurements of the relative positions of the two stars with the best-fit astrometric orbit. Points measured by speckle interferometry are plotted with open circles, micrometer measurements are plotted with dots, and the Hipparcos measurement is shown with a cross. Lines connect measurements to the points on the visual orbit corresponding to their times of observation. The point of periastron on the orbit is marked with a filled black circle.

Table 3
The Stellar Parameters of HD 81809 A and HD 81809 B as Deduced from the Orbital and Spectroscopic Analysis

	HD 81809 A		HD 81809 B
$M/M_\odot$ [a]	0.92 ± 0.09		0.79 ± 0.06
M_A/M_B		1.16 ± 0.07	
$T_{\rm eff}$ (K)	5580 ± 140		5520 ± 150
$v \sin i$ (km s^{-1})	4.0 ± 0.5		4.0 ± 0.5
$\log g$ (dex)	3.8 ± 0.5		4.2 ± 0.5
ξ (km s^{-1})	1.1 ± 1.7		1.0 ± 1.5

Note.
[a] Covariance cov$(M_A/M_\odot, M_B/M_\odot) = 0.0039$.

Furthermore, we identified spectral lines suitable for the determination of the abundances of 27 chemical elements, including Fe. This list is reported in the Appendix (Table A2). We derived the abundances by spectral synthesis, minimizing the χ^2 difference between the observed and synthetic spectra. Synthetic spectra were generated in three steps: (i) plane-parallel local thermodynamic equilibrium atmospheric models were computed using the ATLAS9 code (R. L. Kurucz 1993); (ii) stellar spectra were synthesized using SYNTHE (R. L. Kurucz & E. H. Avrett 1981); and (iii) the synthetic spectra were convolved with instrumental ($R = 85{,}000$) and rotational velocity broadening profiles to match observed line profiles. (iv) The total synthetic spectrum has been computed following G. Catanzaro et al. (2024), using the equation

$$F^{\rm th}_{\rm Tot} = \frac{l_\lambda F^{\rm th}_{\rm A} + F^{\rm th}_{\rm B}}{1 + l_\lambda}, \quad (1)$$

where $F^{\rm th}_{\rm A,B}$ are the synthetic fluxes of the primary and secondary and the luminosity ratio $l_\lambda = (T_{\rm eff,A}/T_{\rm eff,B})^4 (R_A/R_B)^2 \simeq 3.05$ is calculated from the M, $T_{\rm eff}$ and $\log g$ of the single stars reported in Table 3.

The results are shown in Figure 4 and in Table 4, which are given in terms of a ratio both with H and Fe. The chemical properties of HD 81809 A and B provide important results on the scenario of the formation and evolution of this binary system.

The abundance patterns of the two components of HD 81809 reveal a marked chemical difference. The primary (HD 81809 A) is metal poor, with an iron abundance of [Fe/H] $\simeq -0.57$, while the secondary (HD 81809 B) has essentially solar metallicity ([Fe/H] $\simeq 0.00$).

For the primary, most of the measured chemical species—in particular C, Na, and Mg—are underabundant in [X/H] relative to the solar reference values (N. Grevesse et al. 2011), with the notable exception of oxygen, which shows a slight over-abundance of ∼0.16 dex. The abundance distribution, represented by the histogram in the right panel of Figure 4, yields an average metallicity of [M/H] $= -0.44$. The α elements such as Mg, Si, S, and Ca show clear enhancements relative to iron, with typical [X/Fe] values in the range ∼0.2–0.4 dex, consistent with an α-enhanced, chemically older population. This suggests rapid formation in an environment where chemical enrichment occurred on short timescales and was dominated by Type II supernovae (originating from massive stars), before Type Ia supernovae (which mainly produce iron) had a major impact on the chemical composition.

These chemical signatures, combined with the star's kinematic properties, $U = -42.9$, $V = -46.8$, and $W = -2.0$ km s^{-1} (C. Soubiran & P. Girard 2005), which correspond to a total space velocity of ∼63 km s^{-1} relative to the local standard of rest, further support that the star, and hence the system, belongs to an old stellar population, most likely the Galactic thick disk (B. Anguiano et al. 2020; K. Vieira et al. 2022). In addition, the negative V component indicates a lag with respect to Galactic rotation, which is also characteristic of thick-disk stars.

Iron-peak elements (Cr, Mn, Ni, Cu, and Zn) in HD 81809 A are generally subsolar in [X/H], but their [X/Fe] ratios are near solar values, indicating behavior similar to iron. Neutron-capture elements (Sr, Y, Zr, Ba, La, Ce, Nd, and Sm) are also subsolar in [X/H], but tend to be mildly enhanced in [X/Fe], suggesting a moderate enrichment in s-process material relative to iron.

In contrast, HD 81809 B displays abundances much closer to solar for most species, with [X/H] and [X/Fe] typically within a few hundredths of a dex of the solar values. The

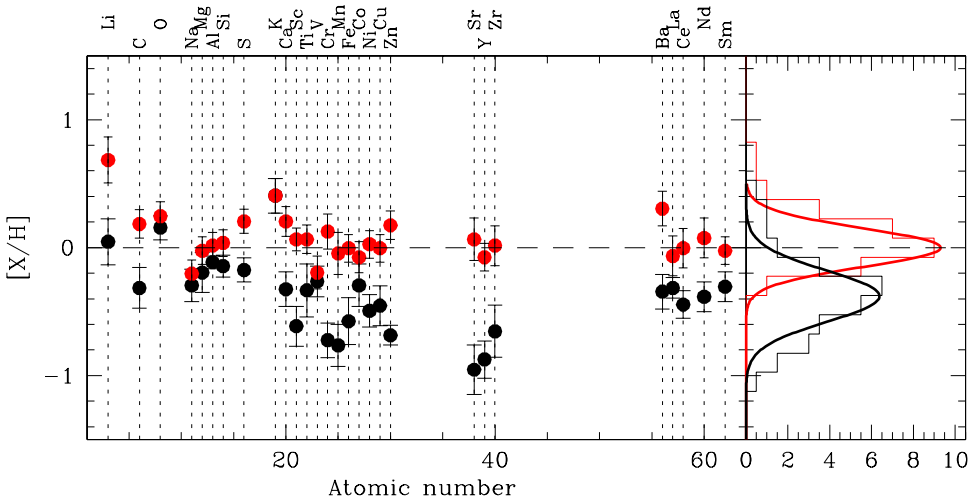

Figure 4. Atmospheric abundances obtained by present analysis for HD 81809 A (black dots) and HD 81809 B (red dots) compared with those of the Sun (N. Grevesse et al. 2011, dashed line). In the right panel, we show histograms of the distribution of the abundances around the average with overplotted Gaussian fit, using the same colors as in the left panel.

Table 4
Atmospheric Abundances for Both Components HD 81809 A and B, for All Identified Elements, Including Those of the Iron Group and the Neutron-capture Elements

	HD 81809 A		HD 81809 B	
Element	[X/H]	[X/Fe]	[X/H]	[X/Fe]
Li	−0.05 ± 0.18	0.62 ± 0.24	0.69 ± 0.18	0.69 ± 0.24
C	−0.31 ± 0.16	0.26 ± 0.24	0.19 ± 0.11	0.19 ± 0.16
O	0.16 ± 0.09	0.73 ± 0.21	0.25 ± 0.11	0.25 ± 0.16
Na	−0.29 ± 0.13	0.28 ± 0.22	−0.20 ± 0.11	−0.20 ± 0.15
Mg	−0.19 ± 0.16	0.38 ± 0.24	−0.02 ± 0.11	−0.02 ± 0.15
Al	−0.11 ± 0.05	0.46 ± 0.19	0.02 ± 0.10	0.02 ± 0.15
Si	−0.14 ± 0.09	0.43 ± 0.20	0.04 ± 0.10	0.04 ± 0.15
S	−0.17 ± 0.09	0.40 ± 0.21	0.21 ± 0.09	0.21 ± 0.14
K	0.41 ± 0.13	0.98 ± 0.23	0.41 ± 0.13	0.41 ± 0.17
Ca	−0.32 ± 0.14	0.25 ± 0.23	0.21 ± 0.12	0.21 ± 0.16
Sc	−0.61 ± 0.16	−0.04 ± 0.24	0.07 ± 0.09	0.07 ± 0.14
Ti	−0.33 ± 0.21	0.24 ± 0.28	0.07 ± 0.11	0.07 ± 0.16
V	−0.26 ± 0.12	0.31 ± 0.22	−0.19 ± 0.13	−0.19 ± 0.17
Cr	−0.72 ± 0.14	−0.15 ± 0.23	0.13 ± 0.14	0.13 ± 0.17
Mn	−0.76 ± 0.16	−0.19 ± 0.25	−0.04 ± 0.16	−0.04 ± 0.20
Fe	−0.57 ± 0.18	...	0.00 ± 0.11	...
Co	−0.29 ± 0.17	0.28 ± 0.25	−0.07 ± 0.12	−0.07 ± 0.16
Ni	−0.49 ± 0.13	0.08 ± 0.22	0.03 ± 0.11	0.03 ± 0.15
Cu	−0.45 ± 0.16	0.12 ± 0.24	−0.00 ± 0.11	−0.00 ± 0.15
Zn	−0.68 ± 0.08	−0.11 ± 0.20	0.18 ± 0.11	0.18 ± 0.16
Sr	−0.95 ± 0.19	−0.38 ± 0.27	0.07 ± 0.17	0.07 ± 0.20
Y	−0.87 ± 0.15	−0.30 ± 0.23	−0.07 ± 0.11	−0.07 ± 0.15
Zr	−0.65 ± 0.20	−0.08 ± 0.27	0.02 ± 0.16	0.02 ± 0.19
Ba	−0.34 ± 0.13	0.23 ± 0.23	0.31 ± 0.13	0.31 ± 0.17
La	−0.31 ± 0.08	0.26 ± 0.20	−0.06 ± 0.16	−0.06 ± 0.19
Ce	−0.44 ± 0.11	0.13 ± 0.21	−0.00 ± 0.16	0.00 ± 0.19
Nd	−0.38 ± 0.12	0.19 ± 0.22	0.08 ± 0.16	0.08 ± 0.19
Sm	−0.30 ± 0.12	0.27 ± 0.22	−0.02 ± 0.11	−0.02 ± 0.15

Note. Columns list abundances in the standard logarithmic form relative to hydrogen and scaled to solar values ([X/H]), and abundances relative to iron ([X/Fe]).

secondary therefore appears chemically normal, while the primary is both more metal poor and α enhanced. This chemical dichotomy between the two components points to a complex evolutionary history for the system and will be further discussed in the next sections.

Lithium was also measured from the Li I 6707.8 Å feature for both components. The primary (HD 81809 A) shows a lithium abundance consistent with the solar value, indicating that only modest depletion has occurred despite the star's evolved state. In contrast, the secondary (HD 81809 B) exhibits a significantly higher lithium abundance, about 0.69 dex above the solar value. This behavior is noteworthy, as lithium is typically depleted in solar-type stars over gigayear timescales. The enhanced abundance in HD 81809 B may

Table 5
Observed Magnitudes and Flux Ratios for HD 81809 and Predicted Values Based on Our Synthetic Photometry

Band	λ_{pivot} (nm)	Observed	Computed	$O - C$
UVW2	213.6	11.018 ± 0.010	10.974 ± 0.049	+0.043 ± 0.050
UVM2	232.7	10.780 ± 0.072	10.546 ± 0.062	+0.234 ± 0.095
m_{2365}	236.3	10.560 ± 0.160	10.858 ± 0.136	−0.298 ± 0.210
m_{2740}	273.9	8.930 ± 0.030	9.174 ± 0.085	−0.244 ± 0.090
U_G	345.5	6.583 ± 0.010	6.552 ± 0.017	+0.031 ± 0.019
$B1_G$	401.9	6.277 ± 0.010	6.286 ± 0.018	−0.009 ± 0.021
B_T	421.2	6.196 ± 0.014	6.194 ± 0.014	+0.002 ± 0.020
B_G	423.9	5.208 ± 0.009	5.220 ± 0.017	−0.012 ± 0.019
B	439.8	6.040 ± 0.010	6.050 ± 0.008	−0.010 ± 0.013
V_T	533.5	5.483 ± 0.009	5.466 ± 0.014	+0.017 ± 0.017
$V1_G$	540.7	6.122 ± 0.010	6.130 ± 0.008	−0.008 ± 0.013
V	550.0	5.390 ± 0.010	5.389 ± 0.004	+0.001 ± 0.011
V_G	550.2	5.377 ± 0.009	5.391 ± 0.012	−0.014 ± 0.015
Hp	550.7	5.503 ± 0.005	5.533 ± 0.011	−0.029 ± 0.012
G_G	581.3	6.418 ± 0.010	6.413 ± 0.016	+0.005 ± 0.019
R	655.6	5.020 ± 0.010	5.006 ± 0.004	+0.014 ± 0.011
I	804.6	4.660 ± 0.010	4.640 ± 0.009	+0.020 ± 0.014
J	1240.6	3.984 ± 0.180	4.130 ± 0.015	−0.146 ± 0.181
H	1649.0	3.586 ± 0.176	3.818 ± 0.019	−0.232 ± 0.177
K_s	2162.9	3.568 ± 0.176	3.766 ± 0.030	−0.198 ± 0.179
S9W	9097.2	8.268 ± 0.002	8.271 ± 0.053	−0.003 ± 0.053
L18W	19507.0	9.788 ± 0.003	9.778 ± 0.070	+0.010 ± 0.070
Flux ratios				
$(F_B/F_A)_{B_T}$	421.2	0.172 ± 0.004	0.172	0.000 ± 0.004
$(F_B/F_A)_{V_T}$	533.5	0.175 ± 0.002	0.176	−0.000 ± 0.002

Note. The predicted magnitudes are shown with error estimates from the uncertainty on the zero-points for each photometric system. The pivot wavelength for each bandpass is shown in the column headed λ_{pivot}. U_G, B_G, etc., are magnitudes in the Geneva seven-color photometry system. TD1 fluxes have been converted to AB magnitudes, e.g., F2365 to m_{2365}.

therefore reflect either a younger evolutionary status compared to the primary, a different internal mixing history, or possible recent accretion events affecting its surface composition. The marked lithium difference between the two stars reinforces the chemical dichotomy observed in this system and may provide additional constraints on its formation and evolutionary history.

2.4. Luminosities from Bolometric Fluxes

The luminosities of the two components were determined from their bolometric fluxes using the TEB software package (N. J. Miller et al. 2020; P. F. L. Maxted et al. 2025). This tool allows a self-consistent analysis of multiband photometry and flux ratios to recover the bolometric fluxes, effective temperatures, and luminosities of the individual stars in binary systems.

We fitted the observed broadband photometry of the unresolved system together with the measured flux ratios in the Tycho B_T and V_T bands (Table 5). The spectral energy distributions (SEDs) used in the analysis are semiempirical, consisting of BT-Settl model atmospheres (F. Allard et al. 2013) multiplied by a smooth function. This approach allows for the SEDs to contain realistic stellar absorption features, but the overall shapes of the SEDs are determined by the observed magnitudes and flux ratios of the binary system. In addition, we used empirical color–T_{eff} relations to ensure that the optical–infrared and near-UV–optical colors computed from the SEDs are similar to those of others stars of the same effective temperature. The derived bolometric fluxes and luminosities are largely insensitive to the assumed stellar radii and effective temperatures, owing to the strong observational constraints imposed by the multiwavelength photometry.

The used photometric dataset given in Table 5 includes measurements from the near-UV to the mid-infrared: *J*, *H*, and *K*s magnitude from the Two Micron All Sky Survey (M. F. Skrutskie et al. 2006); B_T and V_T magnitudes from the Tycho-2 catalog (E. Høg et al. 2000); H_p from the Hipparcos mission (F. van Leeuwen 2007); Geneva seven-color photometry from E. Paunzen (2022); Akari S9W and L18W mid-infrared fluxes from D. Ishihara et al. (2010); *UVM2* and *UVW2* magnitudes from the XMM-Newton Optical Monitor Serendipitous Source Survey Catalog, version 6.0 (M. J. Page et al. 2012); *BVRI* photometry from M. S. Bessel (1990); and near-UV F2365 and F2740 fluxes from the TD1 mission (A. Boksenberg et al. 1973). It is worth noticing that the two stars of the HD 81809 system have not been resolved in Gaia DR3, and the corresponding flag (RUWE = 4.91) is above the recommended threshold for a trustworthy astrometric solution. Therefore, we decided not to use the Gaia *G* magnitude as input.

We adopted the Gaia DR3 parallax ($\pi = 32.32 \pm 0.36$ mas) corrected for the zero-point offset following M. A. T. Groenewegen (2021). For the color excess we used the value $E(B - V) = 0.0054 \pm 0.0011$ from the `bayestar17` Galactic reddening 3D maps (G. M. Green et al. 2018). This negligible reddening value is consistent with the lack of interstellar Na I absorption in the spectra (P. F. L. Maxted 2025) and is expected for stars less than 40 pc from the Sun (J. Holmberg et al. 2007).

The observed and synthetic fluxes and the best-fit SEDs are shown in Figure 5. The luminosities and effective temperatures

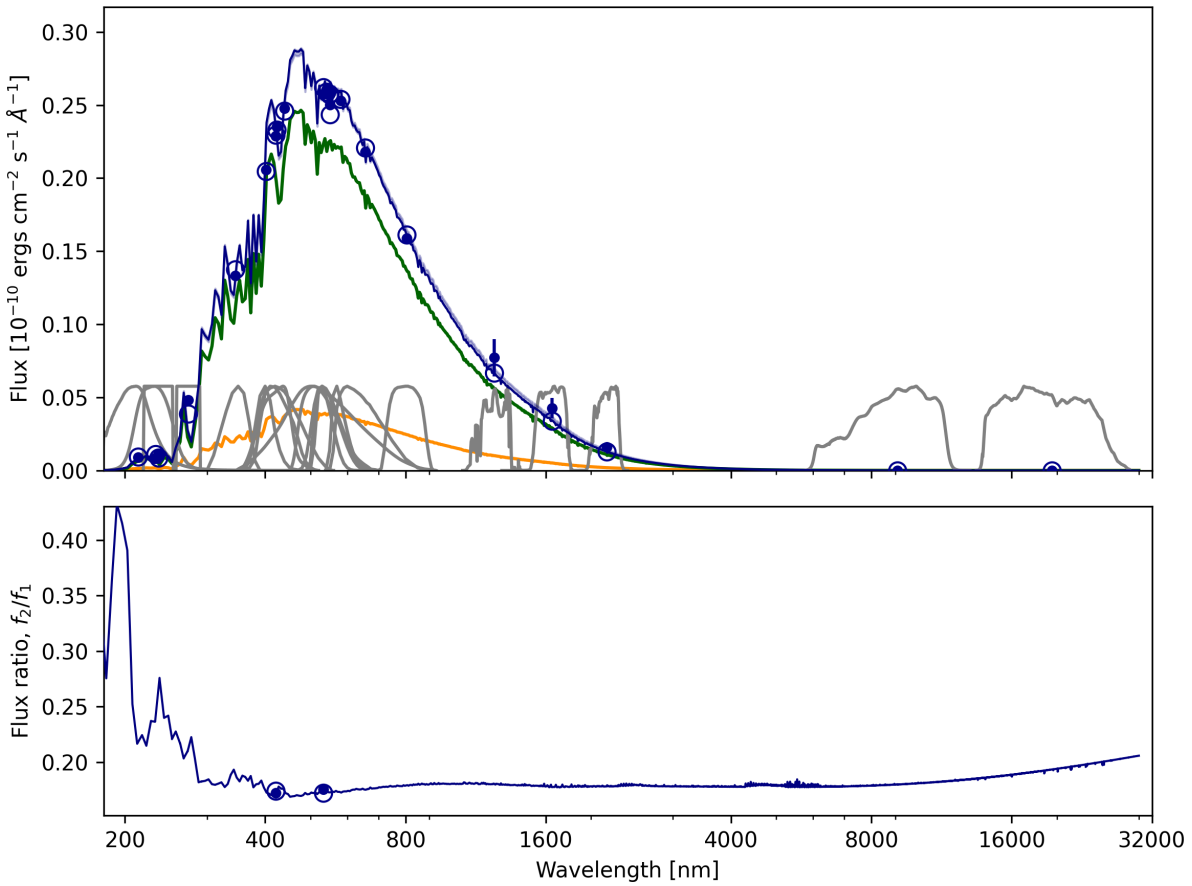

Figure 5. In the upper panel the SED of HD 81809 is shown. The best-fit SED is plotted as the blue line. The observed fluxes are plotted as blue points with error bars while predicted fluxes for the best-fit SED integrated over the response functions shown in gray are plotted with open circles. The SEDs of the two stars are also plotted (green—primary, orange—secondary). Lower panel: flux ratio as a function of wavelength for the best-fit SEDs. The observed flux ratios are plotted as points and the predicted flux ratios in the Tycho B_T and V_T bands are plotted as open circles.

Table 6
Stellar Parameters from the Photometric Analysis

Parameter	HD 81809 A	HD 81809 B
$T_{\rm eff}$ (K)	5554 ± 120	5481 ± 120
$L/L_{\odot}$	5.10 ± 0.14	0.92 ± 0.05

Table 7
IRAS Flux Densities and Infrared Excess Analysis

Band	$\lambda_{\rm pivot}$ (μm)	$F_{\rm obs}$ (arbitrary units)	$F_{\rm mod}$ (arbitrary units)	Excess ($F_{\rm obs}/F_{\rm mod}$)
IRAS 25	25	2.47 ± 0.26	2.32	1.07 ± 0.11
IRAS 60	60	22.6 ± 9.0	7.42	3.05 ± 1.21
IRAS 100	100	191.3 ± 67.7	3.89	49.1 ± 17.4

Note. The observed fluxes ($F_{\rm obs}$) are compared with the photospheric model predictions ($F_{\rm mod}$). The excess ratio ($F_{\rm obs}/F_{\rm mod}$) clearly indicates the presence of cold dust radiating at $\lambda \geqslant 60\,\mu$m. Flux values are scaled by 10^{16} (25 μm), 10^{18} (60 μm), and 10^{19} (100 μm) for readability. The uncertainties on the excess ratio include the observational errors.

obtained from this analysis are given in Table 6. It should be pointed out that while the effective temperatures results in good agreement with the spectroscopic values of Table 3, the ratio between the luminosities $L_{\rm A}/L_{\rm B} \sim 5.54$ is higher than the ratio $l_{\lambda} \sim 3.05$ deduced spectroscopically.

The SED analysis reveals excellent agreement between the observed fluxes and the photospheric models from the UV down to the mid-infrared (AKARI L18W, 19.5 μm), as shown in Table 5. However, a strong infrared excess becomes evident at longer wavelengths $\lambda > 30\,\mu$m in the flux ratio profile, which may be interpreted as evidence for the presence of a cold debris disk which could surround one of the two stars (S-type orbits circumprimary or circumsecondary) or could orbit around the center of mass (P-type orbits circumbinary). We used data from the IRAS Point Source Catalog (G. Helou & D. W. Walker 1988), to pinpoint the thermal properties of the dust (see Table 7). At 60 μm, the observed flux is approximately 3 times higher than the predicted photospheric value, while at 100 μm, the stellar contribution is negligible. Fitting these infrared residuals with a blackbody function yields a characteristic dust temperature of $T_{\rm BB} \simeq 96.6$ K.

Belts of rocks and dust, known as debris disks are commonly detected around main-sequence stars. However, very little is known regarding the debris disks around subgiants, as well as for the evolutionary stage of the primary. It is not clear whether the presence of debris disks correlates with the presence of planets (A. Moro-Martín et al. 2007; G. Bryden et al. 2009; Á. Kóspál et al. 2009).

The presence of a debris disk provides a plausible explanation for the observed metallicity difference between the two stars. While the primary remains metal poor, the

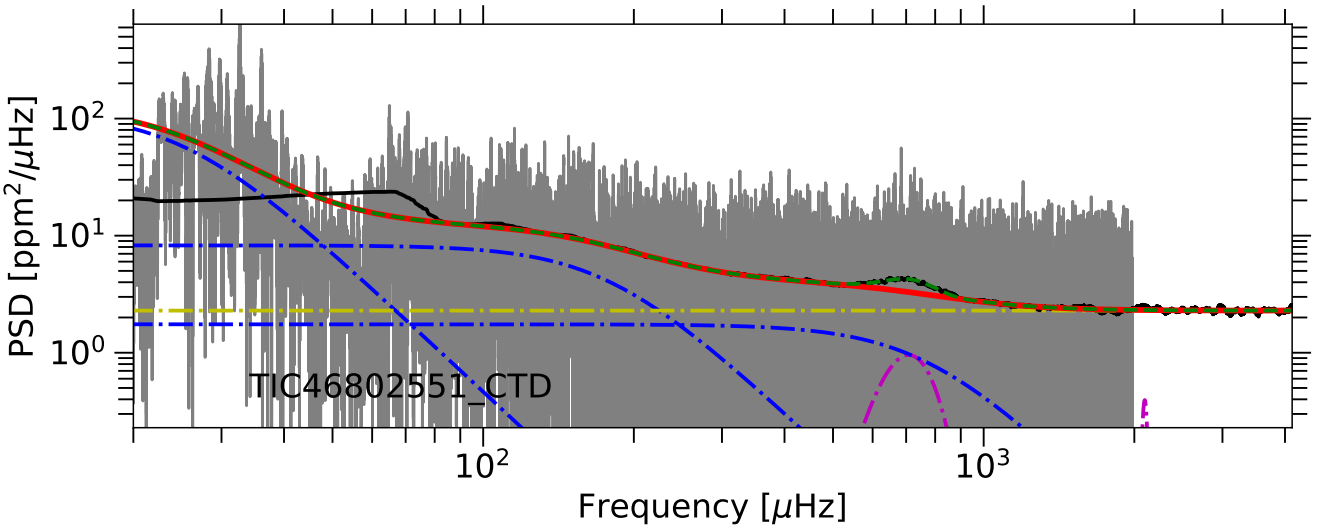

Figure 6. Power spectral density (gray) for HD 81809 observed by TESS during three different years (2021, 2023, and 2025) for 27 days each at 120 s cadence. The excess of power (green line) is calculated by subtracting all the background noise, which include white and colored noise. The estimated background level is shown in red, while the inclusion of the Gaussian power excess is marked by a green dashed line. The individual Harvey-like components are plotted in blue, while the level of the white noise is indicated by the dotted–dashed yellow line.

secondary exhibits nearly solar metallicity, which could result from selective accretion of metal-rich solids from the disk during past dynamical evolution. Such accretion is more effective for stars with shallower convective envelopes and could naturally enhance the photospheric metallicity of the secondary, leaving the primary largely unaffected. This scenario supports the idea that the system experienced significant planetesimal evolution and the possible inward transport of solids, consistent with the detection of the debris disk.

3. Analysis of TESS Asteroseismic Data

3.1. Global Pulsation Properties

HD 81809 has been photometrically observed by TESS during 27 consecutive days in three different years: 2021, 2023, and 2025 in long cadence at 120 s sampling (TESS Team 2021b), and in 2025 also in short cadence at 20 s (TESS Team 2021a). The two components are blended in the TESS observations, with the primary producing a clear detectable asteroseismic signal because of its brightness.

Nonetheless, a careful analysis of the seismic light curve using the public tool DIAMONDS developed by E. Corsaro & J. De Ridder (2014) allowed us to detect an excess of power due to solar-like oscillations not only for the bright primary component, located at $\simeq$700 μHz, but also for the faint secondary component, which, thanks to the adoption of the concatenated time series in short cadence, from 2021 to 2025, was found to be detectable around $\simeq$2100 μHz. In this way it was possible to identify the global pulsation parameters of both components. The resulting global oscillation properties derived for HD 81809 are shown in Table 8. The primary component shows a frequency of maximum oscillation power $\nu_{\rm max} = 708.74^{+3.23}_{-3.74}$ μHz, with a corresponding maximum amplitude of oscillation $A_{\rm max} = 2.84 \pm 0.95$ ppm, and a value for the large frequency separation of $\Delta\nu = 43.32 \pm 3.91$ μHz derived using the methodology presented in E. Corsaro et al. (2024), which is also well compatible with the results previously published by E. Corsaro et al. (2024), who used only one sector of TESS short cadence data. For HD 81809 B we obtain $\nu_{\rm max} = 2098.07^{+3.07}_{-2.83}$ μHz and $\Delta\nu = 97.75 \pm 4.49$ μHz, the latter also derived through an autocorrelation function as presented in E. Corsaro et al. (2024). The detection of the power excess for the secondary component was performed by means of a Bayesian model comparison, following the approach described by E. Corsaro et al. (2024), where the resulting background fitting model is shown in Figure 6, consisting of three Harvey-like components, white noise, and two separate Gaussian envelopes. It is clear that a set of individual oscillation frequencies would have helped to better constrain this target. For this purpose we also attempted to identify individual oscillation modes through the automated pipeline FAMED (E. Corsaro et al. 2020), but the high complexity of the oscillation pattern caused by the presence of avoided crossings and the low signal-to-noise ratio of the region of the power excess could not lead us to a solution.

Table 8
Asteroseismic Global Parameters from the Analysis of the TESS Time Series

Parameter	HD 81809 A	HD 818091 B
$\nu_{\rm max}$ (μHz)	$708.74^{+3.23}_{-3.74}$	$2098.07^{+3.07}_{-2.83}$
$\Delta\nu$ (μHz)	43.32 ± 3.91	97.75 ± 4.49
$A_{\rm max}$ (ppm)	2.84 ± 0.95	⋯

4. Physical Parameters through Stellar Modeling

4.1. Best-fitting Procedure

To characterize the properties of the two stellar components in the HD 81809 system, we employed a global minimization procedure based on classical spectroscopic, asteroseismic, and observed luminosity constraints derived in the previous sections. The adopted minimization procedure employs the Stellar Parameters Inferred Systematically (SPInS) software (Y. Lebreton & D. R. Reese 2020), which is based on an MCMC approach and Bayesian statistics to derive probability distribution functions for the stellar fundamental parameters (age, mass, radius, and initial composition). In this context, we

used two grids of stellar models for the derivation of the fundamental parameters with SPInS: one computed by means of Code Liegeois d'Evolution Stellaire (CLES; R. Scuflaire et al. 2008), and one computed by means of Modules for Experiments in Stellar Astronomy (MESA; B. Paxton et al. 2013, 2015, 2018, 2019). The MESA inlist used in this work is available in Zenodo at DOI: 10.5281/zenodo.18404205.

To determine the fundamental parameters and best-fit models of HD 81809 A and B, given the remarkably large difference in their chemical composition and Fe content (as shown in Table 4), we decided to perform the modeling of the two components independently. Modeling the two components together in the assumption of a common initial chemical composition and age, would lead to an inferred initial abundance of helium $Y_i \sim 0.36$, which is unrealistically large. In this context, two main explanations can be considered to interpret this result: the physics included in the models lacks accuracy, for instance in the computation of the opacity tables or implementation of the transport mechanisms, preventing correct reproduction of the properties of the two components; the two stars may have formed as binary system, and subsequently accreted metal-rich material from a debris disk (as revealed from the SED), which would have been mixed within the stellar interiors in a different manner, given the diverse structure and evolutionary stage of the two components; and it is also possible that the stars formed in chemically different environments, and that they merged into a binary system after formation, due to dynamical interaction. Given the impossibility to select the most probable hypothesis concerning the formation and evolution of the system, we decided to proceed in the modeling by considering one star at the time, and attempt to find physically meaningful solutions.

As first step, for each component we attempted to determine their fundamental parameters (M, R, age, etc.) by considering the whole set of observational constraints derived in the above sections, namely L from Table 6; $T_{\rm eff}$, $\log g$, and [Fe/H] from Table 3; and $\nu_{\rm max}$ and $\Delta\nu$ from Table 8, as input for SPInS. Again, also in this case, SPInS failed to converge toward a physically meaningful solution for either component, in any of the considered stellar model grids presented above. For instance, in the modeling of the primary, we found a solution that would fit the observed bolometric luminosity, but overestimating the mass by about $\sim$0.3 $M_\odot$ and the effective temperature by approximately 300 K (with respect to the value indicated in Table 3). While these values for the mass and effective temperature are compatible with the ones found by K. Fuhrmann & R. Chini (2018), they result to be in disagreement with the orbital masses deduced in Section 2.2. A similar issue is encountered when modeling the secondary component, for which the software tends to converge toward solutions with unrealistically advanced ages, and/or an unrealistically large Y_i.

Thus, we decided to exclude the bolometric luminosity from the set of observational constraints, and in the case of the secondary, we applied two modeling approaches.

1. *B1*. Secondary formed with an initial metallicity independent from primary, constrained by observed [Fe/H] $= 0.00 \pm 0.11$.
2. *B2*. Secondary formed with the $[{\rm M/H}]_0$ inferred from modeling the primary, under the hypothesis of same progenitor cloud.

In the following subsections, we provide a detailed description of the optimal models for HD 81809 A and B obtained with the two aforementioned stellar evolution codes.

4.2. Derivation of Fundamental Stellar Parameters Based on CLES Models

In this section we provide a brief description of the input physics included in the CLES models for the computation of the grid provided to SPInS. For a more detailed description of the physics included in the code, we refer the interested reader to R. Scuflaire et al. (2008). The setup of the input physics employed for the computation of the CLES stellar tracks included: the FreeEOS (A. W. Irwin 2012) equation of state, AGSS09 (M. Asplund et al. 2009) abundances, specifically for the primary component we considered α-enhanced ($\langle[\alpha/{\rm Fe}]\rangle = +0.3$) abundances, and OPAL (C. A. Iglesias & F. J. Rogers 1996) opacity tables (for α-enhanced solar mixture in the case of the primary star). The effects of microscopic diffusion (A. A. Thoul et al. 1994; C. Paquette et al. 1986) and turbulence at the base of the convective envelope were also taken into account. For the outer boundary conditions we employed those of J. E. Vernazza et al. (1981). The classical mixing-length theory was applied for convection, with solar calibrated values $\alpha_{\rm MLT} = 1.93$.

The results obtained with the modeling procedures for HD 81809 A and B are indicated on Table 9, under the flag "CLES." The best-fit parameters found for the primary component are $M = (0.87 \pm 0.08)\,M_\odot$, age $= 9.75 \pm 1.78$ Gyr, $R = (1.95 \pm 0.08)\,R_\odot$, and initial metallicity $[{\rm M/X}]_0 = -0.3898 \pm 0.3169$. The solution we found is able to fit all the observational constraints, except for the luminosity, as explained in the above section. The properties of the best-fit stellar models for HD 81809 A and HD 81809 B are indicated in Table 10.

The two minimization procedures (B1 and B2) applied to the secondary component yield models with significantly different stellar parameters, among which the stellar masses are particularly different. When adopting the observed surface metallicity of HD 81809 B as a constraint, labeled as case B1, the model converges toward the observed effective temperature and global seismic parameters. The observed luminosity is not reproduced. However, the inferred mass results $M_{\rm B} = (0.94 \pm 0.07)\,M_\odot$, which is formally larger than the mass derived for the primary component. The resulting mass difference between model A and model B1 is $\Delta M = 0.07\,M_\odot$ which corresponds to an inconsistency at the $\sim 0.7\sigma$ level. Although this difference can be considered not statistically significant, this formally implies that the hierarchical configuration of the system is physically implausible, as the secondary component is expected to be less massive than the primary.

In contrast, the minimization assuming the initial $[{\rm M/H}]_0$ inferred from the modeling of the primary yields a mass of $M_{\rm B} = (0.83 \pm 0.01)\,M_\odot$, lower than that of the primary and therefore fully consistent with the binary configuration. Nevertheless, this solution overestimates both the effective temperature and the large frequency separation.

Figure 7 shows the evolutionary tracks of the best-fit models for HD 81809 A and HD 81809 B, with the latter corresponding to the two possible fitting solutions, B1 and B2.

Table 9
Stellar Fundamental Parameters for HD 81809 A and B from Stellar Modeling Employing Two Different Evolutionary Codes

		HD 81809 A	HD 81809 B	
Code	Parameters		B1	B2
CLES	Age (Gyr)	9.75 ± 1.78	12.84 ± 2.96	11.13 ± 1.51
	$[M/H]_0$ (dex)	−0.3898 ± 0.3169	0.1387 ± 0.2318	−0.1390 ± 0.2149
	M ($M_\odot$)	0.87 ± 0.08	0.94 ± 0.07	0.83 ± 0.01
	R ($R_\odot$)	1.95 ± 0.08	1.18 ± 0.04	1.12 ± 0.03
	$T_{\rm eff}$ (K)	5619 ± 125	5586 ± 116	5833 ± 72
	log(g) (dex)	3.7981 ± 0.0054	4.2682 ± 0.0454	4.2776 ± 0.0027
	[Fe/H] (dex)	−0.4857 ± 0.1426	0.0510 ± 0.0995	−0.2312 ± 0.0583
	L ($L_\odot$)	3.44 ± 0.43	1.2 ± 0.14	1.31 ± 0.10
	$\Delta\nu$ (μHZ)	46.32 ± 1.05	102.43 ± 1.81	106.21 ± 1.29
	$\nu_{\rm max}$ (μHZ)	708.58 ± 3.76	2098.04± 3.09	2097.95 ± 3.07
	Z_i	0.0051 ± 0.0015	0.0177 ± 0.0038	0.0092 ± 0.0011
	Y_i	0.3002 ± 0.0318	0.2737 ± 0.0294	0.2866 ± 0.0243
MESA	Age (Gyr)	10.21 ± 2.71	15.77 ± 4.11	10.68 ± 0.48
	$[M/H]_0$ (dex)	−0.4599 ± 0.1313	0.1087 ± 0.0999	−0.3712 ± 0.0484
	M ($M_\odot$)	0.88 ± 0.10	0.89 ± 0.08	0.83 ± 0.01
	R ($R_\odot$)	1.97 ± 0.10	1.16 ± 0.05	1.09 ± 0.01
	$T_{\rm eff}$ (K)	5539 ± 119	5466 ± 119	6044 ± 41
	log(g) (dex)	3.7870 ± 0.0052	4.2565 ± 0.0048	4.2781 ± 0.0016
	[Fe/H] (dex)	−0.5140 ± 0.1382	0.0467 ± 0.1038	−0.4503 ± 0.0507
	L ($L_\odot$)	3.33 ± 0.51	1.09 ± 0.16	1.28 ± 0.03
	$\Delta\nu$ (μHZ)	45.62 ± 1.17	102.00 ± 2.05	107.74 ± 0.62
	$\nu_{\rm max}$ (μHZ)	708.53 ± 3.70	2097.94 ± 3.05	2097.80 ± 3.06
	Z_i	0.0047 ± 0.0015	0.0172 ± 0.0039	0.0067 ± 0.0006
	Y_i	0.2875 ± 0.0279	0.2753 ± 0.0254	0.2856 ± 0.0051

Note. For the secondary we considered two different solutions: B1 using the observed [Fe/H] (see Table 3) and B2 using the $[M/H]_0$ deduced by modeling the primary.

Table 10
Stellar Fundamental Parameters for the Best-fit Models of HD 81809 A and B Obtained with Two Different Evolutionary Codes

Model	Component	χ^2	$M/M_\odot$	$R/R_\odot$	$L/L_\odot$	$T_{\rm eff}$ (K)	log(g) (dex)	$\Delta\nu$ (μHz)	$\nu_{\rm max}$ (μHz)	$r_{\rm cz}/R$	$X_{\rm c}$	$(Z/X)_{\rm s}$	Age (Gyr)	$(Z/X)_0$ (dex)
CLES	A	0.35	0.93	2.02	3.55	5570	3.79	45.40	710.85	0.57	1.61×10^{-23}	0.0047	9.58	0.0064
	B1	0.71	0.95	1.19	1.24	5580	4.27	101.67	2096.99	0.67	1.74×10^{-3}	0.015	14.31	0.023
	B2	18.0	0.87	1.12	1.35	5886	4.28	106.22	2096.24	0.72	8.04×10^{-3}	0.0081	11.11	0.013
MESA	A	0.23	0.96	2.07	3.649	5546	3.79	44.56	708.90	0.524	9.68×10^{-44}	0.0050	9.10	0.0055
	B1	1.88	0.95	1.20	1.165	5477	4.26	100.31	2098.10	0.640	6.33×10^{-4}	0.0194	14.53	0.0220
	B2	3.50	0.83	1.09	1.435	6050	4.28	107.85	2098.08	0.707	3.00×10^{-3}	0.0066	10.69	0.0077

4.3. Fundamental Stellar Parameters by Using SPInS-MESA

In order to confirm the obtained results, we performed a characterization of HD 81809 using stellar models computed by MESA (B. Paxton et al. 2013, 2015, 2018, 2019). We produced the global minimization by applying SPInS to a stellar models grid with characteristics similar to those of grid C of N. Moedas et al. (2025), extended to lower metallicity to cover the parameters space of the studied stars. The input physics differs from that of the CLES stellar modeling, because here we adopted the OPAL2005 equation of state (F. J. Rogers & A. Nayfonov 2002), and no α enhancement for the primary.

The results, shown in Table 9 for the primary component are $M = (0.88 \pm 0.10)\,M_\odot$, age $= 10.21 \pm 2.71$ Gyr, stellar radius $R = (1.97 \pm 0.1)\,R_\odot$, and initial metallicity $[M/X]_0 = -0.4599 \pm 0.1313$. As already pointed out for the CLES models, the observed and modeled luminosities differ by about 3.3σ, which is statistically significant.

The two minimization procedures applied to the secondary component yield models with different stellar parameters (see Table 9). When adopting the observed surface metallicity of HD 81809 B, the model converges toward the observed luminosity, effective temperature, and global seismic parameters. However, the inferred mass $M_{\rm B} = (0.89 \pm 0.08)\,M_\odot$ is formally larger than the mass derived for the primary component, with a difference between MESA models A and B1 of $\Delta M = 0.01\,M_\odot$. This indicates that the masses are statistically indistinguishable and hence consistent with the expected binary configuration. The inferred age is 15.77 ± 4.11 Gyr, with a rather large uncertainty that likely overestimates the true error and formally exceeds the age of the Universe. This apparent overestimation likely reflects the large uncertainties in the observational constraints, and degeneracies between stellar parameters. Therefore, while the age indicates an old system, the absolute value obtained with MESA should be interpreted with caution.

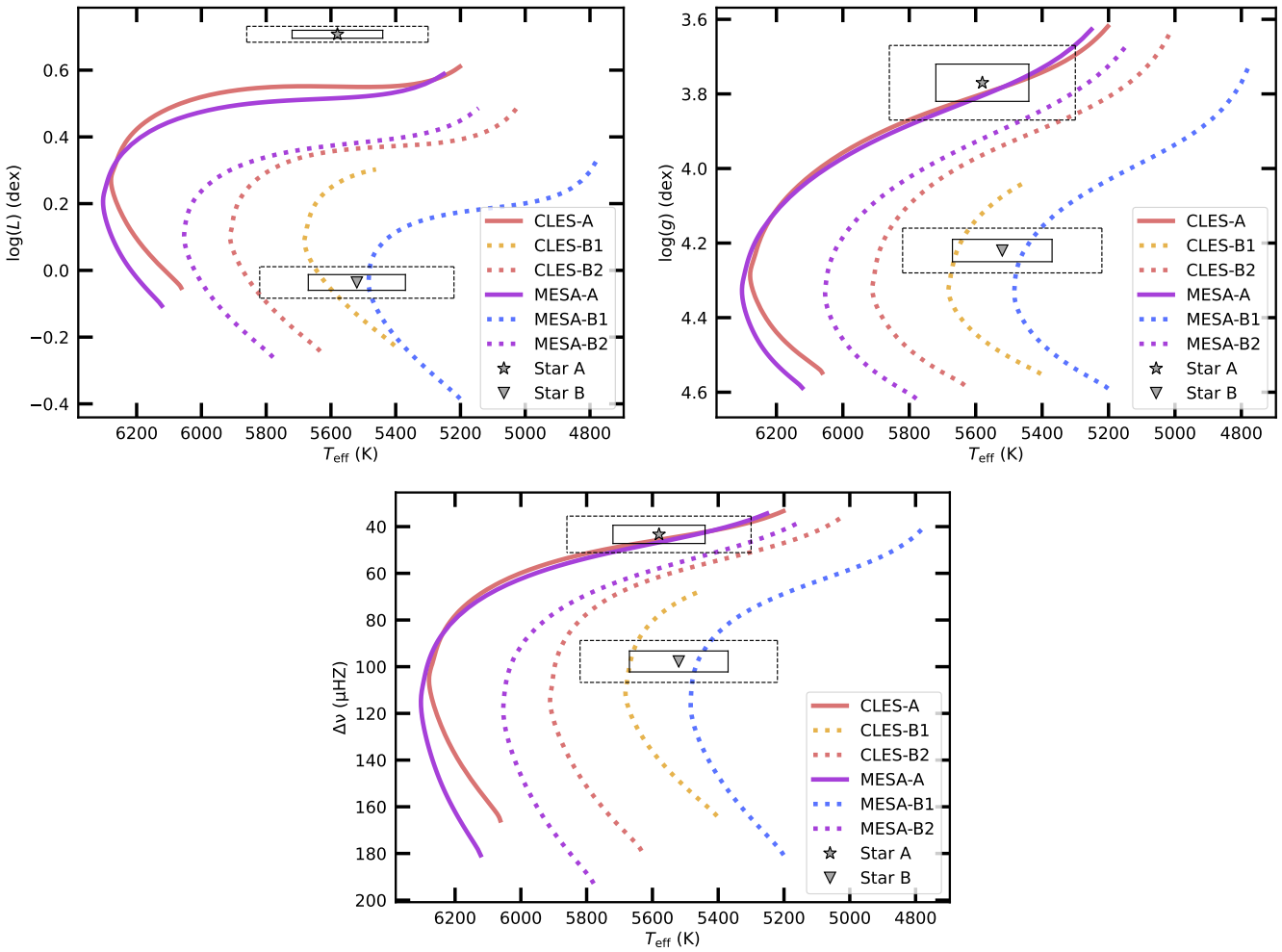

Figure 7. Hertzsprung–Russell (top left panel), Kiel (top right panel), and seismic (bottom panel) diagrams showing the evolutionary tracks of the best-fit stellar models for HD 81809 A (solid lines) and HD 81809 B (dotted lines) with the parameters given in Table 10. The star and the triangle shows the correspondent observed parameters for the two components, and the solid and the dashed line boxes correspond to the 1σ and 2σ errors, respectively.

The minimization assuming the initial $[M/H]_0$ inferred from modeling the primary yields a mass of $M_B = (0.83 \pm 0.01)\,M_\odot$, lower than that of the primary and therefore fully consistent with the binary configuration, an age $= 10.68 \pm 0.48$ Gyr, and a stellar radius $R = (1.09 \pm 0.01)\,R_\odot$ (see Table 9).

The properties of the best-fit stellar models of the two components are indicated in Table 10 with the flag "MESA."

4.4. The Modeling Results: Discrepancies and Preferred Solutions

According to the present modeling obtained with two different evolutionary codes, the system is composed by a main component with mass $M_A \sim 0.88\,M_\odot$ and radius $R_A \sim 1.96\,R_\odot$ that has exhausted the hydrogen content in the core, has already passed the turn-off, and is currently on the subgiant branch (see Figure 7) as indicated by the hydrogen content in the core X_c. The convective envelope is deeper than that of the Sun with a base located at $r_{cz} \sim (0.5{-}0.6)\,R$. The slightly smaller mass companion is instead in the main-sequence phase.

The results obtained for the two components, as an average of the results obtained with the two codes, indicate that the system is old with an age ~ 10 Gyr, as expected from the observed high value of [Mg/Fe] of the primary. This result is in disagreement with the one obtained by K. Fuhrmann & R. Chini (2018; see Section 1).

The lithium depletion profiles, shown for the best models from CLES and MESA in Figure 8, provide additional information on the ages of the stars. For HD 81809 A, the tracks show very steep Li depletion occurring during the subgiant phase, in a relatively short evolutionary time. The observed stellar value, indicated by the gray region, is consistent with an age ~ 10 Gyr. The Li tracks of the secondary (right panel of Figure 8) show that this star, due to its low mass, should have lost its initial Li during its main-sequence life. On the contrary, the observed abundance of Li shows that it is still relatively Li rich, with an observed [Li/H] $= 0.69$ dex. The possible explanations are planet engulfment, suppressed depletion due to low rotational mixing, or an unusual internal structure.

Nevertheless, the comparison between the observed and modeled properties of HD 81809 reveals other notable differences, particularly for the primary component. The observed luminosity, $L/L_\odot = 5.10 \pm 0.14$, is significantly higher than the one predicted by both the CLES ($L/L_\odot = 3.44 \pm 0.43$) and MESA ($L/L_\odot = 3.33 \pm 0.51$) models, corresponding to about a 3.5σ discrepancy. This difference might likely arises from a combination of factors, including uncertainties in the input physics of stellar models (e.g., opacities, convective efficiency, composition, and treatment of

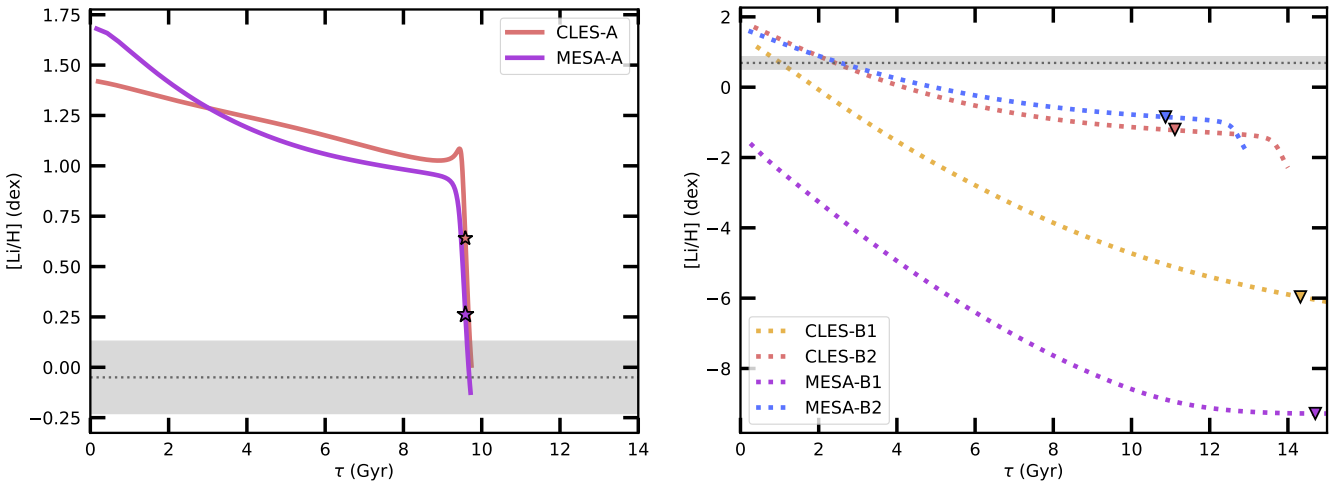

Figure 8. Lithium evolution in the CLES and MESA models for HD 81809 A (left panel) and HD 81809 B (right panel). The black dotted line shows the observed [Li/H] value, and the gray region shows its uncertainty. The stars and triangles indicate location of the best-fit models of Table 10.

α-enhanced composition), rapid luminosity evolution in the subgiant phase, and potential systematic uncertainties in the observed luminosity. In particular, the nonsolar α-enhanced composition of HD 81809 A suggests that standard solar-scaled models may not fully capture the stellar structure, indicating caution when interpreting absolute luminosities.

For the secondary component, the modeling considering the observed surface metallicity (B1 solution) yields slightly overestimated masses, exceeding the primary's mass (CLES: $M_{\rm B} = (0.94 \pm 0.07)\, M_{\odot}$ versus MESA: $M_{\rm B} = (0.89 \pm 0.08)\, M_{\odot}$). This value is physically inconsistent for a hierarchical binary.

Under the assumption of a common initial chemical composition for the system, adopting as initial metallicity the one derived from the primary (B2 solution), the best-fitting produces masses fully consistent with the expected binary hierarchy ($M_{\rm B} \sim 0.83 \pm 0.01\, M_{\odot}$ with both the evolutionary codes). Notably, this value is in good agreement with the independently observed dynamical masses derived from the orbital analysis and also with the ratio measurement $M_{\rm A}/M_{\rm B}$ given in Table 1. Nevertheless, we point out that this solution led to models that do not fully reproduce the observed luminosity, effective temperature, and the asteroseismic large separation.

5. Analysis of Stellar Magnetic activity

HD 81809 was part of the largest and longest observational campaign to monitor the magnetic activity of Sun-like stars, conducted at the Mount Wilson Observatory (MWO; O. C. Wilson 1968, 1978). The available dataset[7] consists of 1879 individual measurements obtained between 1966 and 2001 using the HKP spectrophotometer at the MWO. The data are expressed in terms of the dimensionless S-index, which represents the most widely used stellar activity proxy. The MWO S-index is based on the intensity of emission in the chromospheric Ca II H (393.3 nm) and K (396.8 nm) lines cores normalized to that two nearby continuum reference bandpasses, as follows:

$$S_{\rm MWO} = \alpha \frac{N_{\rm H} + N_{\rm K}}{N_R + N_V}, \tag{2}$$

where $N_{\rm H}$ and $N_{\rm K}$ are the counts in 1.09 Å triangular bands centered on Ca II H and K, respectively, while N_R and N_V are 20 Å reference bandpasses in the nearby continuum region, and α is a calibration factor (see O. C. Wilson 1978; A. H. Vaughan et al. 1978, for further details).

Monitoring the chromospheric activity of this star was subsequently continued with the Solar-Stellar Spectrograph (SSS) at the Lowell Observatory (J. C. Hall & G. W. Lockwood 1995), resulting in 362 additional measurements over the time interval 1993–2018. Thanks to the combined dataset from the two observatories, it has been possible to study the magnetic activity of this star over nearly 52 yr (1966–2018), making it one of the stars whose magnetic activity has been most closely monitored. The presence of a time interval with overlapping data from both MWO and Lowell SSS allows us to intercalibrate the two datasets. To this aim, we first removed outliers from both datasets, excluding those outside $\pm 4\sigma$ of the average, and then applied the relation provided by R. Egeland (2017) to calibrate the Lowell SSS S-index to the MWO S-index scale.

The S-index time series plotted in the top panel of Figure 9 indicates that from the MWO data $S_{\rm MWO} = 0.172 \pm 0.010$, while from the Lowell SSS data (once calibrated to the MWO scale) $S_{\rm Lowell} = 0.170 \pm 0.010$, which confirms the previous estimate by R. Egeland (2018). It is interesting to note that while this star shows higher variability in the S-index ($\sim$0.05) —i.e., the difference between the maximum and minimum values—compared to the Sun during a solar cycle ($\simeq$0.02), its mean activity level is consistent with the average solar S-index value over the last 10 solar cycles $S = 1.01\, S_{\odot}$ (see R. Egeland et al. 2017, for the solar value). To analyze the activity cycle of this star, which appears to exhibit clear periodicity based on the S-index measurements, we performed a Lomb–Scargle analysis (N. R. Lomb 1976; J. D. Scargle 1982). The results of this analysis (Figure 9), performed separately on both the MWO and Lowell time series, indicate a main cycle of 8.15 yr for the former and 8.09 yr for the latter. The results are highly consistent, and when the two time series are merged, the analysis indicates the presence of an unambiguous main activity cycle of $\sim$8.18 yr.

The result is in good agreement with the periodicity of 7.3 ± 1.5 yr obtained by S. Orlando et al. (2017) for the X-ray luminosity, based on XMM-Newton data. However, it should be noted that the shorter average cycle observed in the X-ray activity may be influenced by the fact that it is derived from

[7] https://dataverse.harvard.edu/dataverse/mwo_hk_project

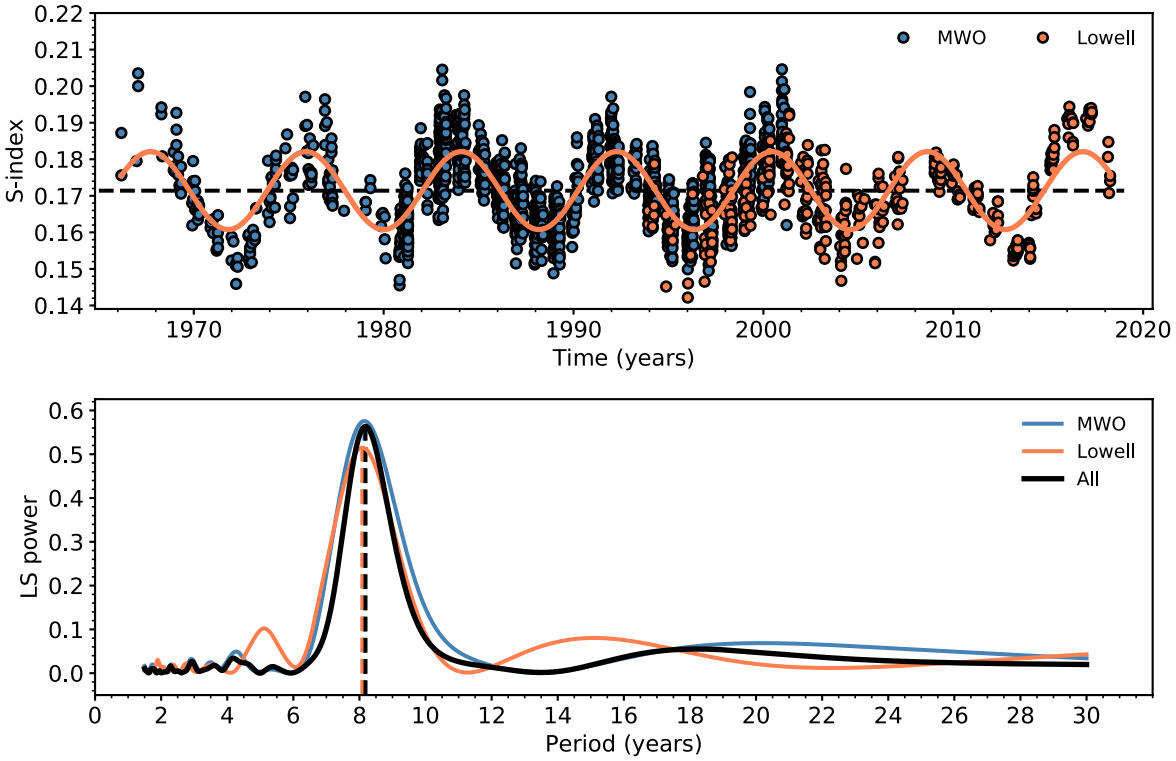

Figure 9. Top: *S*-index measurements of HD 81809 from MWO (blue points) and Lowell SSS (orange points), with the dashed black line indicating the average *S*-index value. The orange curve represents a sinusoidal fit to the highest peak of the periodogram, as shown in the bottom panel. Bottom: Lomb–Scargle periodogram of the MWO and Lowell SSS time series, along with the periodogram obtained by merging the two datasets (black line).

only 15 yr of data (2001 November–2016 October), a time interval considerably shorter than the 50 yr of chromospheric activity. The clear periodical signal retrieved for HD 81809 indicates that the variability is dominated by only one component of the binary. The other component has either flat or a negligible activity with respect to the primary.

It is interesting to show that although the Lomb–Scargle analysis reveals the presence of additional lower-amplitude modulations, the dominance of the main cycle places this star in the faculae-dominated activity regime, similar to the Sun. Stars in this regime exhibit photospheric and chromospheric variabilities that are nearly in phase. For HD 81809 A, this is further corroborated by T. Reinhold et al. (2019), who reported a phase difference of $\Delta\phi = 0.08 \pm 0.01$ between photometric and chromospheric time series.

As shown by decades of observations at Mount Wilson, subgiant stars rarely exhibit activity cycles (S. L. Baliunas et al. 1995). The rotation and cycle period ($P_{\rm cyc}$) of HD 81809 places it on the so-called "inactive" branch (E. Böhm-Vitense 2007), which is characterized by a shallower slope in the $P_{\rm cyc}$–$P_{\rm rot}$ relationship. The fact that this subgiant shows a magnetic activity cycle provides an interesting constraint on its stellar dynamo evolution. According to T. S. Metcalfe & J. van Saders (2017), activity cycles are expected to lengthen progressively with increasing rotation period. This behavior can be explained by the fact that as a star evolves from zero-age main sequence and approaches the so-called critical Rossby number (J. L. van Saders et al. 2016), its rotation period remains relatively constant, while the activity cycle becomes longer and weaker before disappearing entirely. The results obtained for this subgiant suggest that it may have had a relatively short activity cycle until it reached the so-called critical Rossby number. Beyond this point, the cycle should have then grown longer and weaker at a nearly constant Rossby number. When hydrogen core burning ceased, the core likely contracted and the star became hotter, developing a thinner convection zone. This would have pushed it above the critical Rossby number, resulting in a transition to a "flat activity" state. However, with the onset of hydrogen shell burning, the star would have begun to expand and cool, further slowing its rotation through the conservation of angular momentum and deepening the outer convection zone. These evolutionary effects can push the Rossby number back below $Ro_{\rm crit} = (0.92 \pm 0.01)\, Ro_{\odot} = 1.656 \pm 0.02$ (T. S. Metcalfe et al. 2024) with $Ro_{\odot}$ from F. A. Rasio et al. (1996) so the star can reinvigorate large-scale dynamo action and briefly sustain an activity cycle before ascending the red giant branch as found by T. S. Metcalfe et al. (2020), A. R. G. Santos et al. (2025).

6. Rotational and X-Ray Luminosity Evolution of HD 81809 A

In the comprehensive study of the HD 81809 system conducted by R. Egeland (2018), the authors concluded that the convolved rotational period and the magnetic activity cycle, determined through the in-phase variability of the *S*-index and X-ray luminosity observed for HD 81809, can be reasonably attributed to the subgiant component of the system.

To test the compatibility of the best-fit stellar model of the primary star derived in this work with the observational data for the rotational period and X-ray luminosity, we computed postprocessed rotational and X-ray luminosity tracks of HD 81809 A, by providing the CLES evolutionary tracks derived from the best-fit stellar modeling in Section 4 to SPI, a star–planet interaction code (C. Pezzotti et al. 2025). In this code, the evolution of the stellar surface rotation rate is computed under the assumption of solid-body rotation, by

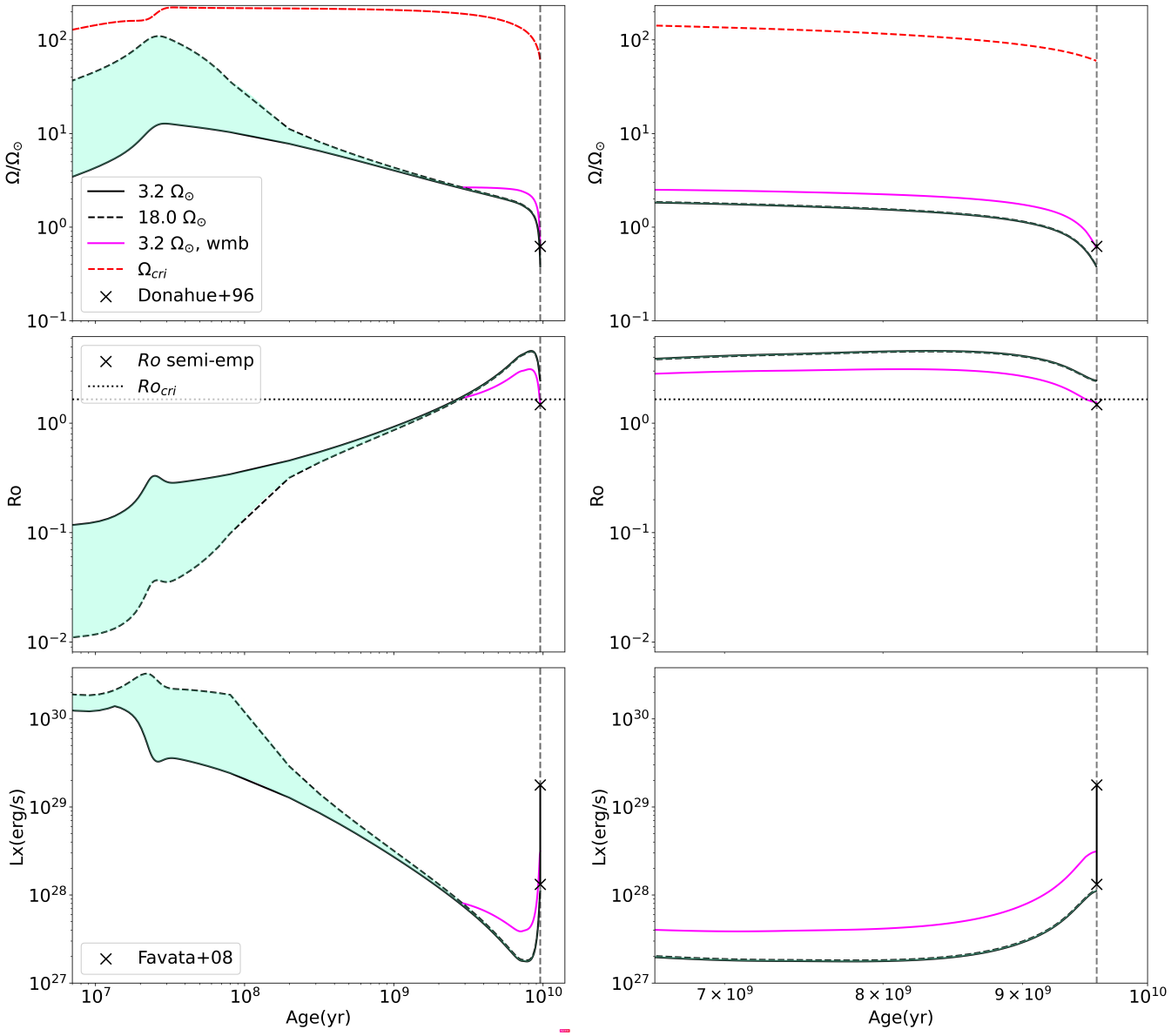

Figure 10. Evolution of the surface rotation rate, Rossby number, and X-ray luminosity computed for HD 81809 A. In the panels on the right, zoom-in views of regions of interest are shown. The green shaded area indicates the region of variation of the surface rotation rate across the evolution of the star, for initial values ranging between 3.2 and 18 $\Omega_{\odot}$. The red dashed line shows the evolution of the critical rotational velocity ($\Omega_{\rm crit}$), defined as the velocity at which the centrifugal acceleration at the equator equals gravity. The purple line is obtained in the hypothesis that the star switched into a weakened magnetic braking at an age of 2 Gyr, for an initial value of the surface rotation rate 3.2 $\Omega_{\odot}$. The black crosses represent the observational values, as indicated in the legend. The observed variation in the X-ray luminosity emitted by the system over a magnetic cycle, with the minimum and maximum indicated by the black crosses, is taken from F. Favata et al. (2008).

accounting for the braking of the stellar surface due to magnetized winds as in S. P. Matt et al. (2015, 2019). Given the degeneracy in the rotational history of solar-like low-mass stars, we considered initial values of the surface rotation rate ranging between 3.2 and 18 times the surface rotation rate of the Sun at solar age ($\Omega_{\odot} = 2.9 \times 10^{-6}$ rads^{-1}), to account for the spread of surface rotation rates observed for stars in young cluster and stellar associations (F. Gallet & J. Bouvier 2015).

For initial surface rotation rates in the range $\Omega_{\rm in} < 18\,\Omega_{\odot}$, a disk-locking timescale of 6 Myr was assumed, while for $\Omega_{\rm in} = 18\,\Omega_{\odot}$ the assumed disk-locking timescale was 2 Myr. For values of the stellar Rossby number above the critical value $Ro_{\rm crit} > 0.92\,Ro_{\odot}$ (T. S. Metcalfe et al. 2024), it is possible to switch into a "weakened magnetic braking" regime (J. L. van Saders et al. 2016). In this circumstance, the braking due to magnetized winds is simply turned off.

The local convective turnover timescale at the base of the convective zone is computed as in F. A. Rasio et al. (1996) and E. Villaver & M. Livio (2009). The evolution of the stellar X-ray luminosity is computed consistently to the one of the surface rotation rate, by following a recalibration of the $R_{\rm X}$ vs *Ro* prescription (C. P. Johnstone et al. 2021), as in C. Pezzotti et al. (2021), where $R_{\rm X}$ is the ratio between the X-ray to the bolometric luminosity. For a more detailed description of the physics included in the star–planet interaction code, we refer the interested reader to C. Pezzotti et al. (2025).

In Figure 10 (left panel, from top to bottom) we show the evolution of the surface rotation rate, the stellar Rossby number, and the X-ray luminosity as a function of time for the

tracks corresponding to the best model of HD 81809 A. The right panels show a zoom-in view of the region of potential overlap between the tracks and the observational data.

The evolutionary stage at which the onset of the weakened magnetic braking occurs is indicated in the middle panel, by the crossing between the tracks and the horizontal dotted line, which is the critical threshold ($Ro_{\rm crit}$) by T. S. Metcalfe et al. (2024). In this figure, it is possible to notice that, at the estimated age of the system (age $\simeq 9.58$ Gyr), the models accounting for weakened magnetic braking (purple line) result in agreement with the observations of stellar surface rotation (R. A. Donahue 1993; R. A. Donahue et al. 1996) and the emitted X-ray luminosity (F. Favata et al. 2008). As discussed in Section 5, indeed a decrease in the Rossby number is visible in the middle panel in correspondence of the end of the main sequence and the subsequent overall contraction, which could have eventually caused "rejuvenation" of the dynamo at work in the stellar interior, with a reborn magnetic cycle and increase of the $L_{\rm X}$ emission.

7. Discussion and Conclusions

In this work, we have presented a multidisciplinary characterization of the binary system HD 81809, combining high-resolution spectroscopy, precise RVs, Gaia astrometry, TESS asteroseismology, and decades of magnetic activity monitoring. By integrating these diverse datasets with advanced stellar evolutionary modeling (CLES and MESA), we establish HD 81809 as a unique benchmark for stellar physics, particularly regarding the evolution of old, metal-poor stars and the interplay between rotation, accretion, and magnetic activity.

7.1. Evolutionary Status and Membership

The joint orbital and asteroseismic analysis confirms that HD 81809 is a long-period binary ($P \simeq 34.5$ yr) composed of two solar-like stars. The primary (HD 81809 A, $M \simeq 0.88\,M_{\odot}$) has evolved off the main sequence and is currently crossing the subgiant branch, while the secondary (HD 81809 B, $M \simeq 0.83\,M_{\odot}$) lays on the main sequence.

The revised atmospheric parameters derived in this study resolve previous inconsistencies regarding the system's age and population membership. The kinematic properties of the system, combined with the clear α enhancement ($[\alpha/{\rm Fe}] \simeq +0.3$) and low metallicity ($[{\rm Fe/H}] \simeq -0.57$) of the primary component, strongly suggest that HD 81809 belongs to the Galactic thick-disk population. This is further corroborated by the present asteroseismic age estimates, which consistently point to an old system with an age of $\simeq$10 Gyr. This makes HD 81809 one of the nearest and brightest accessible laboratories for studying the physics of old, metal-poor stars.

The result reconciles the tension found in previous investigations (e.g., K. Fuhrmann & R. Chini 2018), where the high [Mg/Fe] ratio and slow rotation suggested an old age that conflicted with younger isochrone fits.

It is important to acknowledge that the current stellar models do not yield a perfect statistical fit to all observational constraints. First, both the CLES and MESA codes underestimate the bolometric luminosity of the primary by approximately $\sim 3.5\sigma$. This discrepancy likely stems from a combination of limitations in the input physics for evolved, α-enhanced stars (e.g., opacity tables or mixing-length calibrations) and potential systematic effects in the observed photometry due to contamination by the circumstellar debris disk.

Furthermore, another significant modeling challenge arises because the secondary star is an "impostor." Its surface composition does not reflect its internal structure, breaking the standard assumptions of stellar evolution models. In fact, when models are forced to match the observed solar-like surface metallicity ($[{\rm Fe/H}] = 0.00$), they predict a mass that is physically impossible, because it is higher than the evolved primary star: the models compensate for the high metallicity by increasing the mass, violating the binary hierarchy. When models use the true initial metallicity inferred from the primary ($[{\rm Fe/H}] = -0.57$), they correctly recover the low mass, but fail to match the observed effective temperature and seismic large separation. These mismatches highlight the inherent challenge of modeling "polluted" stars using standard evolutionary tracks, which do not account for the stratification and specific structural changes caused by the accretion of metal-rich material onto a metal-poor envelope.

7.2. The Chemical Dichotomy and the Accretion Hypothesis

One of the most striking results of this study is the significant chemical discrepancy between the two components. While the primary exhibits a composition typical of old, metal-poor thick-disk stars, the secondary displays a solar-like metallicity ($[{\rm Fe/H}] \simeq 0.0$) and a remarkably high lithium abundance ($[{\rm Li/H}] \simeq 0.69$ dex above solar).

We interpret this dichotomy as the signature of a pollution event. The presence of a significant infrared excess ($\lambda > 30\,\mu$m) detected in the SED analysis indicates the existence of a cold debris disk ($T_{\rm BB} = 96.6$ K) in the system. We propose that the secondary star has undergone recent accretion of metal-rich, planetary material. The difference in the observed photospheric abundances can be explained by the internal structure of the two stars. The primary, being a subgiant, possesses a deepening convective envelope that would rapidly dilute any accreted material, effectively erasing the signature of recent pollution and revealing the pristine, metal-poor natal composition.

In contrast, the main-sequence secondary likely retains a thinner surface convection zone (relative to the expanding subgiant). Consequently, accreted metal-rich material and lithium—likely from the ingestion of rocky planetesimals—remained concentrated on the photosphere, creating the illusion of a younger, solar-metallicity star. The high lithium abundance in the secondary supports the ingestion of rocky, planetesimal material, which can replenish surface Li that is otherwise depleted in old stars.

7.3. Magnetic Rejuvenation in the Subgiant Phase

Our analysis of the 50 yr chromospheric activity record (MWO and SSS data) confirms a magnetic cycle of $P_{\rm cycl} \simeq 8.2$ yr.

Standard dynamo theory suggests that stars moving off the main sequence should spin down and become magnetically "dead." However, HD 81809 A appears to be an example of "dynamo rejuvenation."

As a star evolved off the main sequence, the contraction of the core and the subsequent expansion of the envelope caused

the rotation to slow and the convective zone to deepen. Our evolutionary models and SPI simulations suggest that HD 81809 A has recently evolved back below the critical Rossby number threshold ($Ro < Ro_{crit}$). This structural change has likely reactivated a large-scale $\alpha-\Omega$ dynamo, allowing the star to sustain the coherent, Sun-like activity cycle we observe today. This places HD 81809 A in a crucial, transient evolutionary phase, providing observational evidence for magnetic life after the main sequence.

7.4. Concluding Remarks

HD 81809 has proven to be a unique laboratory for binary evolution study, linking several distinct areas of stellar astrophysics:

1. it validates evolutionary models for metal-poor, α-enhanced stars serving as a probe for the history of the Milky Way's thick disk;
2. it provides a rare case study of chemically peculiar binaries, supporting scenarios of planetesimal engulfment and external pollution; and
3. it offers a detailed look at the reactivation of magnetic dynamos in subgiants, constraining the interaction between rotation, convection, and magnetic fields.

We can conclude that the characterization of HD 81809 provided in this study opens several promising avenues for further investigation. First and foremost, high-resolution spectroscopic monitoring of both components would be essential to disentangle the contribution of the secondary and possibly refine the chemical abundance pattern, including neutron-capture elements, which could offer insight into the early Galactic chemical evolution.

Second, future asteroseismic missions such as PLATO (H. Rauer et al. 2025), with improved temporal coverage and photometric precision, or perhaps ground-based RVs from the SONG network (F. Grundahl et al. 2017) could allow the detection of individual oscillation modes, in order to significantly improve the precision of age and mass estimates.

Furthermore, a dedicated interferometric campaign, with CHARA (e.g., D. Mourard et al. 2015; A. Gallenne et al. 2016) or VLTI (e.g., P. Kervella et al. 2008), could provide direct radius measurements, offering an independent constraint particularly in relation to the debated bolometric luminosities.

Finally, on the magnetic activity front, long-term chromospheric monitoring, possibly combined with new X-ray observations with eROSITA (e.g., J. Robrade et al. 2023) or Athena (e.g., M. Cruise et al. 2025), could help to further constrain the magnetic cycle characteristics and test dynamo models for evolved, metal-poor subgiants. In particular, HD 81809 A offers a unique test bed to study the transition between solar-like dynamos and the weakened magnetic braking regime in evolved stars. High-resolution spectropolarimetry to map the magnetic topology of the primary would be the ultimate test for dynamo models of evolved, metal-poor stars.

Acknowledgments

We acknowledge funding for the publication of the present manuscript and for the position of N.M. from the research theory grant "Synergic tools for characterizing solar-like stars and habitability conditions of exoplanets" (PI: M. P. Di Mauro) under the INAF national call for Fundamental Research 2023.

The authors are thankful to Jeffrey C. Hall for providing the Lowell SSS *S*-index data.

A.B. and E.C. are funded by the European Union–NextGenerationEU RRF M4C2 1.1 n: 2022HY2NSX. "CHRONOS: adjusting the clock(s) to unveil the CHRONO-chemo-dynamical Structure of the Galaxy" (PI: S. Cassisi). We acknowledge support from the research grant "Unveiling the magnetic side of the Stars" (PI: A. Bonanno) funded under the INAF national call for Fundamental Research 2023. C.P. thanks the Belgian Federal Science Policy Office (BELSPO) for the financial support in the framework of the PRODEX Program of the European Space Agency (ESA) under contract number 4000141194.

This publication makes use of VOSA, developed under the Spanish Virtual Observatory project[8] funded by MCIN/AEI/10.13039/501100011033/ through grant PID2020-112949GB-I00. VOSA has been partially updated by using funding from the European Union's Horizon 2020 Research and Innovation Programme, under Grant Agreement no 776403 (EXOPLANETS-A). P.M. acknowledges support from UK Science and Technology Facilities Council (STFC) research grant Nos ST/X002047/1 and ST/Y002563/1.

This study uses spectra obtained with the Hermes spectrograph, installed on the Mercator telescope at the Roque de Los Muchachos observatory on the island of La Palma, operated by the KU Leuven University.

This research has made use of the Keck Observatory Archive (KOA), which is operated by the W. M. Keck Observatory and the NASA Exoplanet Science Institute (NExScI), under contract with the National Aeronautics and Space Administration.

Based on observations made with ESO Telescopes at the La Silla Paranal Observatory under program ID 099.A-9022(A).

Appendix
Astrometric Dataset

Additional observational data, which complement the results discussed in Section 2, are listed in Tables A1 and A2.

[8] https://svo.cab.inta-csic.es

Table A1
Measurements of the Angular Separation (ρ) and Position Angle (θ) of HD 81809 B Relative to HD 81809 A

Year	ρ (arcsec)	θ (deg)	Source	Method	Year	ρ (arcsec)	θ (deg)	Source	Method
1938.16	0.15	−41.0	(1)	M	1989.30	0.412	147.2	(10)	S
1941.25	0.19	−28.3	(1)	M	1989.94	0.438	147.7	(8)	S
1953.03	0.30	143.6	(1)	M	1990.34	0.452	148.0	(8)	S
1955.18	0.37	149.2	(1)	M	1990.34	0.453	148.0	(8)	S
1958.04	0.36	151.6	(1)	M	1990.92	0.475	148.5	(11)	S
1960.21	0.43	150.9	(1)	M	1991.25	0.487	147.6	(12)	H
1962.21	0.42	152.5	(1)	M	1992.30	0.507	148.5	(13)	S
1963.27	0.44	155.7	(1)	M	1993.09	0.528	149.5	(9)	S
1965.06	0.40	158.4	(1)	M	1993.26	0.51	142.1	(14)	M
1976.28	0.29	−28.0	(1)	M	1994.24	0.55	151.2	(15)	M
1976.37	0.289	−26.2	(2)	S	1994.31	0.545	150.3	(11)	S
1977.17	0.300	−25.0	(2)	S	1994.87	0.544	150.1	(9)	S
1977.34	0.295	−25.1	(2)	S	1995.92	0.518	150.7	(16)	S
1977.91	0.302	−28.1	(2)	S	1996.16	0.40	145.6	(17)	M
1977.91	0.258	−22.1	(2)	S	1996.17	0.532	151.0	(9)	S
1980.15	0.188	−19.0	(3)	S	1996.33	0.46	151.2	(18)	M
1982.16	0.033	1.0	(4)	S	1996.87	0.513	151.1	(9)	S
1984.38	0.120	134.1	(5)	S	1997.30	0.470	151.6	(19)	S
1987.26	0.306	144.6	(6)	S	1998.91	0.392	146.5	(16)	S
1988.14	0.31	144.5	(7)	M	1999.16	0.446	153.4	(20)	S
1988.16	0.354	146.3	(8)	S	2009.26	0.264	−32.7	(21)	S
1988.25	0.360	145.8	(6)	S	2011.03	0.3186	−29.6	(22)	S
1988.25	0.364	146.4	(9)	S	2014.18	0.2302	−24.0	(23)	S
1989.22	0.409	146.6	(10)	S	2019.13	0.1255	134.6	(24)	S

Note. The method used for the measurements are indicated as follows: M—micrometer, S—speckle interferometry, and H—Hipparcos. Sources are as follows: (1) P. Baize (1985), (2) H. A. McAlister & E. M. Hendry (1982), (3) H. A. McAlister et al. (1983), (4) I. Balega et al. (1984), (5) H. A. McAlister et al. (1987), (6) H. A. McAlister et al. (1989), (7) W. D. Heintz (1990), (8) H. A. McAlister et al. (1993), (9) W. I. Hartkopf et al. (2000), (10) H. McAlister et al. (1990), (11) W. I. Hartkopf et al. (1996), (12) ESA (1997), (13) W. I. Hartkopf et al. (1994), (14) J. F. Ling & V. Lanchares (1993), (15) A. Alzner (1998), (16) W. I. Hartkopf et al. (1997), (17) C. Prieto (1997), (18) W. D. Heintz (1998), (19) G. G. Douglass et al. (1999), (20) B. D. Mason et al. (2001), (21) A. Tokovinin et al. (2010), (22) W. I. Hartkopf et al. (2012), (23) A. Tokovinin et al. (2015), and (24) A. Tokovinin et al. (2020).

Table A2
Spectral Lines Used for Deriving the Abundances

Line	λ (Å)	log gf	E_{low} (eV)	J_{low}	E_{up} (eV)	J_{up}	Line	λ (Å)	log gf	E_{low} (eV)	J_{low}	E_{up} (eV)	J_{up}
C I	4932.050	−1.658	7.685	1.0	10.198	0.0	S I	4694.113	−1.713	6.524	2.0	9.165	3.0
C I	5052.144	−1.303	7.685	1.0	10.138	2.0	S I	6052.656	−0.672	7.870	3.0	9.918	4.0
C I	5380.325	−1.616	7.685	1.0	9.989	1.0	S I	6743.535	−1.066	7.866	1.0	9.704	2.0
C I	6587.620	−1.003	8.537	1.0	10.419	1.0	S I	6757.153	−0.352	7.870	3.0	9.704	4.0
C I	8335.147	−0.437	7.685	1.0	9.172	0.0	S I	8694.709	0.050	7.870	3.0	9.295	4.0
C I	9061.435	−0.347	7.483	1.0	8.851	2.0	Ca I	6161.297	−1.020	2.523	2.0	4.535	2.0
C I	9062.472	−0.455	7.480	0.0	8.848	1.0	Ca I	6162.173	−0.170	1.899	2.0	3.910	1.0
C I	9094.829	0.151	7.488	2.0	8.851	2.0	Ca I	6166.439	−0.900	2.521	1.0	4.531	0.0
C I	9111.799	−0.297	7.488	2.0	8.848	1.0	Ca I	6169.042	−0.550	2.523	2.0	4.532	1.0
O I	6300.304	−9.776	0.000	2.0	1.967	2.0	Ca I	6462.567	0.310	2.523	2.0	4.441	3.0
O I	7771.944	0.369	9.146	2.0	10.741	3.0	Ca I	6471.673	−8.940	5.228	2.0	7.144	1.0
O I	7774.166	0.223	9.146	2.0	10.740	2.0	Ca I	7148.150	0.307	2.709	2.0	4.443	2.0
O I	7775.388	0.002	9.146	2.0	10.740	1.0	Ca I	7326.144	−5.543	5.732	3.0	7.424	3.0
O I	8446.247	−0.463	9.521	1.0	10.989	0.0	Ca II	8498.020	−1.363	1.692	1.5	3.151	1.5
Na I	4497.656	−1.574	2.104	1.5	4.860	2.5	Ca II	8542.088	−0.411	1.700	2.5	3.151	1.5
Na I	4668.556	−2.264	2.104	1.5	4.759	1.5	Ca II	8662.138	−0.672	1.692	1.5	3.123	0.5
Na I	5682.632	−0.706	2.102	0.5	4.284	1.5	Sc II	5031.021	−0.399	1.357	2.0	3.821	1.0
Na I	5688.204	−0.452	2.104	1.5	4.283	2.5	Sc II	5239.813	−0.765	1.455	0.0	3.821	1.0
Na I	6154.223	−1.547	2.102	0.5	4.116	0.5	Sc II	5526.789	0.025	1.768	4.0	4.011	3.0
Na I	6160.746	−1.246	2.104	1.5	4.116	0.5	Sc II	5657.886	−0.603	1.507	2.0	3.698	2.0
Mg I	4571.096	−5.623	0.000	0.0	2.712	1.0	Sc II	5684.190	−1.074	1.507	2.0	3.687	1.0
Mg I	5167.316	−2.558	5.108	1.0	7.507	2.0	Sc II	6245.621	−1.022	1.507	2.0	3.492	3.0
Mg I	5172.684	−0.393	2.712	1.0	5.108	1.0	Ti I	5512.524	−0.400	1.460	4.0	3.709	3.0
Mg I	5183.604	−0.167	2.717	2.0	5.108	1.0	Ti I	5514.343	−0.660	1.430	2.0	3.678	1.0
Mg I	5711.088	−1.724	4.346	1.0	6.516	0.0	Ti I	5514.534	−0.500	1.443	3.0	3.691	2.0

Table A2
(Continued)

Line	λ (Å)	log gf	E_{low} (eV)	J_{low}	E_{up} (eV)	J_{up}	Line	λ (Å)	log gf	E_{low} (eV)	J_{low}	E_{up} (eV)	J_{up}
Mg I	7691.553	−0.783	5.753	2.0	7.365	3.0	Ti I	5662.152	−0.053	2.318	4.0	4.507	5.0
Mg I	8054.231	−2.238	5.933	2.0	7.472	2.0	Ti I	6258.102	−0.299	1.443	3.0	3.424	4.0
Al I	6696.012	−1.569	3.143	0.5	4.994	1.5	Ti I	6261.099	−0.423	1.430	2.0	3.409	3.0
Al I	6698.662	−1.870	3.143	0.5	4.993	0.5	Ti I	7209.436	−0.430	1.460	4.0	3.179	3.0
Al I	7836.108	−0.534	4.022	2.5	5.603	3.5	Ti I	8412.357	−1.427	0.818	2.0	2.292	1.0
Al I	8772.857	−0.349	4.021	1.5	5.434	2.5	Ti I	8434.954	−0.830	0.848	5.0	2.318	4.0
Al I	8773.888	−0.192	4.022	2.5	5.434	3.5	Ti I	8435.652	−0.967	0.836	4.0	2.305	3.0
Si I	5684.484	−1.733	4.954	2.0	7.134	1.0	Ti II	4805.093	−0.941	2.061	1.5	4.641	0.5
Si I	5690.425	−1.772	4.930	1.0	7.108	1.0	Ti II	5336.786	−1.600	1.582	2.5	3.904	3.5
Si I	5948.541	−0.780	5.082	1.0	7.166	2.0	Ti II	5381.022	−1.970	1.566	1.5	3.869	2.5
Si I	6155.134	−0.755	5.619	3.0	7.633	4.0	Ti II	5418.768	−2.130	1.582	2.5	3.869	2.5
Si I	6237.319	−0.975	5.614	1.0	7.601	2.0	V I	4379.190	0.580	0.301	4.5	3.131	5.5
Si I	6243.815	−1.244	5.616	2.0	7.601	3.0	V I	5698.516	−0.120	1.064	2.5	3.239	3.5
Si I	6244.466	−1.091	5.616	2.0	7.601	3.0	V I	5703.555	−0.210	1.051	1.5	3.224	2.5
Si I	7003.569	−0.939	5.964	2.0	7.734	3.0	V I	6090.194	−0.070	1.081	3.5	3.116	2.5
Si I	7005.880	−0.741	5.984	3.0	7.753	4.0	V I	6243.098	−0.940	0.301	4.5	2.286	4.5
Si I	7034.901	−0.624	5.871	2.0	7.633	3.0	Cr I	4801.025	−0.131	3.122	4.0	5.703	3.0
Si I	7405.772	−0.313	5.614	1.0	7.287	2.0	Cr I	4876.403	−2.483	4.096	2.0	6.638	2.0
Si I	7409.083	−0.620	5.616	2.0	7.289	3.0	Cr I	5204.511	−0.198	0.941	2.0	3.323	1.0
Si I	7423.496	−0.176	5.619	3.0	7.289	4.0	Cr I	5206.037	0.025	0.941	2.0	3.322	2.0
Si I	7424.610	−1.610	5.619	3.0	7.289	3.0	Cr I	5208.425	0.172	0.941	2.0	3.321	3.0
Si I	7932.348	−0.469	5.964	2.0	7.527	3.0	Cr II	4824.131	−0.920	3.871	4.5	6.440	4.5
Si I	7944.001	−0.293	5.984	3.0	7.544	4.0	...	...	...	...	...	...	...
Si I	7970.307	−1.428	5.964	2.0	7.519	2.0	...	...	...	...	...	...	...
Mn I	4754.035	−0.080	2.282	2.5	4.889	3.5	Nd II	5293.163	0.100	0.823	7.5	3.165	6.5
Mn I	4761.504	−0.274	2.953	0.5	5.556	1.5	Nd II	5092.794	−0.610	0.380	5.5	2.814	5.5
Mn I	4762.361	0.304	2.888	3.5	5.491	4.5	Nd II	5688.518	−0.310	0.986	6.5	3.165	6.5
Mn I	4765.856	−0.086	2.941	1.5	5.542	2.5	Sm II	4537.941	−0.480	0.485	6.5	3.216	6.5
Mn I	4783.405	0.044	2.298	3.5	4.889	3.5	Sm II	4577.688	−0.650	0.248	1.5	2.956	2.5
Mn I	4823.506	0.136	2.319	4.5	4.889	3.5	Sm II	4642.228	−0.460	0.378	5.5	3.049	5.5
Mn I	5407.440	−1.743	2.143	3.5	4.435	3.5	Sm II	4566.202	−0.590	0.333	2.5	3.048	2.5
Mn I	5420.425	−1.462	2.143	3.5	4.429	2.5	...	...	...	...	...	...	...
Mn I	6013.453	−0.354	3.072	1.5	5.133	2.5	...	...	...	...	...	...	...
Mn I	6016.632	−0.181	3.073	2.5	5.133	2.5	...	...	...	...	...	...	...
Mn I	6021.788	−0.054	3.075	3.5	5.133	2.5	...	...	...	...	...	...	...
Co I	4118.763	−0.193	1.049	2.5	4.058	3.5	...	...	...	...	...	...	...
Co I	5352.020	0.125	5.892	4.5	3.576	5.5	...	...	...	...	...	...	...
Co I	5369.587	−1.610	1.740	1.5	4.049	2.5	...	...	...	...	...	...	...
Co I	6450.134	−1.850	2.137	3.5	4.058	3.5	...	...	...	...	...	...	...
Co I	6454.958	−0.139	5.552	4.5	3.632	3.5	...	...	...	...	...	...	...
Ni I	4551.224	−0.863	6.891	3.0	4.167	2.0	...	...	...	...	...	...	...
Ni I	4815.922	−1.683	3.542	2.0	6.116	2.0	...	...	...	...	...	...	...
Ni I	5084.089	−0.084	3.678	3.0	6.116	4.0	...	...	...	...	...	...	...
Ni I	5094.411	−0.998	3.833	1.0	6.266	1.0	...	...	...	...	...	...	...
Ni I	5099.922	−0.236	3.678	3.0	6.109	3.0	...	...	...	...	...	...	...
Ni I	5424.635	−2.632	1.951	1.0	4.236	2.0	...	...	...	...	...	...	...
Cu I	5105.512	−1.542	1.389	2.5	3.817	1.5	...	...	...	...	...	...	...
Cu I	5218.194	0.364	3.817	1.5	6.192	2.5	...	...	...	...	...	...	...
Cu I	5153.237	0.116	3.786	0.5	6.191	1.5	...	...	...	...	...	...	...
Cu I	5700.231	−2.583	1.642	1.5	3.817	1.5	...	...	...	...	...	...	...
Cu I	5782.121	−1.905	1.642	1.5	3.786	0.5	...	...	...	...	...	...	...
Cu I	8092.623	−0.131	3.817	1.5	5.348	0.5	...	...	...	...	...	...	...
Zn I	4680.136	−0.810	4.006	0.0	6.655	1.0	...	...	...	...	...	...	...
Zn I	4722.157	−0.338	4.030	1.0	6.655	1.0	...	...	...	...	...	...	...
Zn I	4810.532	−0.125	4.078	2.0	6.655	1.0	...	...	...	...	...	...	...
Sr II	4077.709	0.167	0.000	0.5	3.040	1.5	...	...	...	...	...	...	...
Sr II	4215.519	−0.145	0.000	0.5	2.940	0.5	...	...	...	...	...	...	...
Y II	4883.682	0.070	1.084	4.0	3.622	3.0	...	...	...	...	...	...	...
Y II	4900.119	−0.090	1.033	3.0	3.562	2.0	...	...	...	...	...	...	...
Y II	5087.418	−0.170	1.084	4.0	3.520	4.0	...	...	...	...	...	...	...
Y II	5402.773	−0.360	1.839	2.0	4.133	3.0	...	...	...	...	...	...	...
Zr II	4149.198	−0.040	0.802	3.5	3.789	3.5	...	...	...	...	...	...	...
Zr II	4496.962	−0.890	0.713	2.5	3.470	2.5	...	...	...	...	...	...	...

Table A2
(Continued)

Line	λ (Å)	log *gf*	E_{low} (eV)	J_{low}	E_{up} (eV)	J_{up}	Line	λ (Å)	log *gf*	E_{low} (eV)	J_{low}	E_{up} (eV)	J_{up}
Ba II	4554.029	0.140	0.000	0.5	2.722	1.5	...	...	...	...	...	...	...
Ba II	4934.076	−0.160	0.000	0.5	2.512	0.5	...	...	...	...	...	...	...
Ba II	5853.668	−0.908	0.604	1.5	2.722	1.5	...	...	...	...	...	...	...
Ba II	6141.713	−0.032	0.704	2.5	2.722	1.5	...	...	...	...	...	...	...
Ba II	6496.897	−0.407	0.604	1.5	2.512	0.5	...	...	...	...	...	...	...
La II	5114.556	−1.060	0.235	1.0	2.658	1.0	...	...	...	...	...	...	...
La II	5290.811	−1.750	0.000	2.0	2.343	2.0	...	...	...	...	...	...	...
Ce II	4222.597	−0.150	0.122	4.5	3.058	4.5	...	...	...	...	...	...	...
Ce II	4562.359	0.210	0.478	3.5	3.195	4.5	...	...	...	...	...	...	...

ORCID iDs

Maria Pia Di Mauro https://orcid.org/0000-0001-7801-7484
Camilla Pezzotti https://orcid.org/0009-0009-6066-0194
Nuno Moedas https://orcid.org/0000-0002-2087-6427
Giovanni Catanzaro https://orcid.org/0000-0003-4337-8612
Pierre F. L. Maxted https://orcid.org/0000-0003-3794-1317
Enrico Corsaro https://orcid.org/0000-0001-8835-2075
Raffaele Reda https://orcid.org/0000-0001-8623-5318
Richard Scuflaire https://orcid.org/0009-0000-8017-7962
Alfio Maurizio Bonanno https://orcid.org/0000-0003-3175-9776
Luca Giovannelli https://orcid.org/0000-0001-7369-8516
Paul G. Beck https://orcid.org/0000-0003-4745-2242

References

Allard, F., Homeier, D., Freytag, B., et al. 2013, MSAIS, 24, 128
Alzner, A. 1998, A&AS, 132, 237
Anguiano, B., Majewski, S. R., Hayes, C. R., et al. 2020, AJ, 160, 43
Asplund, M., Grevesse, N., Sauval, A. J., et al. 2009, ARA&A, 47, 481
Bailer-Jones, C. A. L., Rybizki, J., Fouesneau, M., et al. 2021, AJ, 161, 147
Baize, P. 1985, A&AS, 60, 333
Balega, I., Bonneau, D., & Foy, R. 1984, A&AS, 57, 31
Baliunas, S. L., Donahue, R. A., Soon, W. H., et al. 1995, ApJ, 438, 269
Bessel, M. S. 1990, A&AS, 83, 357
Böhm-Vitense, E. 2007, ApJ, 657, 486
Boksenberg, A., Evans, R. G., Fowler, R. G., et al. 1973, MNRAS, 163, 291
Bryden, G., Beichman, C. A., Carpenter, J. M., et al. 2009, ApJ, 705, 1226
Catanzaro, G., Frasca, A., Alonso-Santiago, J., et al. 2024, A&A, 685, A133
Corsaro, E., & De Ridder, J. 2014, A&A, 571, A71
Corsaro, E., McKeever, J. M., & Kuszlewicz, J. S. 2020, A&A, 640, A130
Corsaro, E., Bonanno, A., Kayhan, C., et al. 2024, A&A, 683, A161
Cruise, M., Guaianazzi, M., Aird, J., et al. 2025, NatAs, 9, 36
Donahue, R. A. 1993, PhD thesis, New Mexico State Univ.
Donahue, R. A., Saar, S. H., & Baliunas, S. L. 1996, ApJ, 466, 384
Douglass, G. G., Mason, B. D., Germain, M. E., et al. 1999, AJ, 118, 1395
Egeland, R. 2017, PhD thesis, Montana State Univ.
Egeland, R. 2018, ApJ, 866, 80
Egeland, R., Soon, W., Baliunas, S., et al. 2017, ApJ, 835, 25
ESA 1997, yCat, 1239, 0
Favata, F., Micela, G., Baliunas, S. L., et al. 2004, A&A, 418, L13
Favata, F., Micela, G., Orlando, S., et al. 2008, A&A, 490, 1121
Foreman-Mackey, D., Hogg, D. W., Lang, D., et al. 2013, PASP, 125, 306
Fuhrmann, K., & Chini, R. 2018, ApJ, 858, 103
Gallenne, A., Mérand, A., Kervella, P., et al. 2016, A&A, 586, A70
Gallet, F., & Bouvier, J. 2015, A&A, 577, A98
Green, G. M., Schlafly, E. F., Finkbeiner, D., et al. 2018, MNRAS, 478, 651
Grevesse, N., Asplund, M., Sauval, A., & Scott, P. 2011, CaJPh, 89, 327
Groenewegen, M. A. T. 2021, A&A, 654, A20
Grundahl, F., Fredslund Andersen, M., Christensen-Dalsgaard, J., et al. 2017, ApJ, 836, 142
Hall, J. C., & Lockwood, G. W. 1995, ApJ, 438, 404
Hartkopf, W. I., McAlister, H. A., Mason, B. D., et al. 1994, AJ, 108, 2299
Hartkopf, W. I., Mason, B. D., McAlister, H. A., et al. 1996, AJ, 111, 936
Hartkopf, W. I., McAlister, H. A., Mason, B. D., et al. 1997, AJ, 114, 1639
Hartkopf, W. I., Mason, B. D., McAlister, H. A., et al. 2000, AJ, 119, 3084
Hartkopf, W. I., Tokovinin, A., & Mason, B. D. 2012, AJ, 143, 42
Heintz, W. D. 1990, ApJS, 74, 275
Heintz, W. D. 1998, ApJS, 117, 587
Helou, G., & Walker, D. W. 1988, Infrared Astronomical Satellite (IRAS) Catalogs and Atlases. Volume 7: The Small Scale Structure Catalog NAS 1.61:1190-VOL-7, Jet Propulsion Lab, https://ntrs.nasa.gov/citations/19890004828
Høg, E., Fabricius, C., Makarov, V. V., et al. 2000, A&A, 355, L27
Holmberg, J., Nordström, B., & Andersen, J. 2007, A&A, 475, 519
Iglesias, C. A., & Rogers, F. J. 1996, ApJ, 464, 943
Irwin, A. W. 2012, FreeEOS: Equation of State for stellar interiors calculations, Astrophysics Source Code Library, ascl:1211.002
Ishihara, D., Onaka, T., Kataza, H., et al. 2010, A&A, 514, A1
Johnstone, C. P., Bartel, M., & Güdel, M. 2021, A&A, 649, A96
Kaufer, A., Stahl, O., Tubbesing, S., et al. 1999, Msngr, 95, 8
Kervella, P., Mérand, A., Szabados, L., et al. 2008, A&A, 480, 167
Kóspál, Á., Ardila, D. R., Moór, A., & Ábrahám, P. 2009, ApJL, 700, L73
Kovtyukh, V. V., & Gorlova, N. I. 2000, A&A, 358, 587
Kurucz, R. L. 1993, ASPC, 44, 87
Kurucz, R. L., & Avrett, E. H. 1981, SAOSR, 391
Lebreton, Y., & Reese, D. R. 2020, A&A, 642, A88
Lebreton, Y., Goupil, M. J., & Montalbán, J. 2014, in The Ages of Stars, ed. Y. Lebreton, D. Valls-Gabaud, & C. Charbonnel, 65 (EAS Publications), 177
Ling, J. F., & Lanchares, V. 1993, AN, 314, 303
Lomb, N. R. 1976, Ap&SS, 39, 447
Mason, B. D., Hartkopf, W. I., Holdenried, E. R., et al. 2001, AJ, 121, 3224
Matt, S. P., Brun, A. S., Baraffe, I., et al. 2015, ApJL, 799, L23
Matt, S. P., Brun, A. S., Baraffe, I., et al. 2019, ApJL, 870, L27
Maxted, P. F. L. 2025, RNAAS, 9, 146
Maxted, P. F. L., Miller, N. J., Baycroft, T. A., et al. 2025, MNRAS, 544, 4611
McAlister, H., Hartkopf, W. I., & Franz, O. G. 1990, AJ, 99, 965
McAlister, H. A., & Hendry, E. M. 1982, ApJS, 48, 273
McAlister, H. A., Hendry, E. M., Hartkopf, W. I., et al. 1983, ApJS, 51, 309
McAlister, H. A., Hartkopf, W. I., Hutter, D. J., et al. 1987, AJ, 93, 688
McAlister, H. A., Hartkopf, W. I., Sowell, J. R., et al. 1989, AJ, 97, 510
McAlister, H. A., Mason, B. D., & Hartkopf, W. I. 1993, AJ, 106, 1639
Metcalfe, T. S., & van Saders, J. 2017, SoPh, 292, 126
Metcalfe, T. S., van Saders, J. L., Basu, S., et al. 2020, ApJ, 900, 154
Metcalfe, T. S., Strassmeier, K. G., Ilyin, I. V., et al. 2024, ApJL, 960, L6
Miller, N. J., Maxted, P. F. L., & Smalley, B. 2020, MNRAS, 497, 2899
Moedas, N., Deal, M., & Bossini, D. 2025, A&A, 695, A9
Moro-Martín, A., Carpenter, J. M., Meyer, M. R., et al. 2007, ApJ, 658, 1312
Mourard, D., Monnier, J. D., Ligi, R., et al. 2015, AdSpR, 56, 1707
Orlando, S., Favata, F., Micela, G., et al. 2017, A&A, 605, A19
Page, M. J., Brindle, C., Talavera, A., et al. 2012, MNRAS, 426, 903
Paquette, C., Pelletier, C., Fontaine, G., et al. 1986, ApJS, 61, 177
Paunzen, E. 2022, A&A, 661, A89
Paxton, B., Cantiello, M., Arras, P., et al. 2013, ApJS, 208, 4
Paxton, B., Marchant, P., Schwab, J., et al. 2015, ApJS, 220, 15
Paxton, B., Schwab, J., Bauer, E. B., et al. 2018, ApJS, 234, 34
Paxton, B., Smolec, R., Schwab, J., et al. 2019, ApJS, 243, 10
Pezzotti, C., Eggenberger, P., Buldgen, G., et al. 2021, A&A, 650, A108

Pezzotti, C., Buldgen, G., Magaudda, E., et al. 2025, A&A, 694, A179
Pourbaix, D., Tokovinin, A. A., Batten, A. H., et al. 2004, A&A, 424, 727
Prieto, C. 1997, A&AS, 121, 405
Rasio, F. A., Tout, C. A., Lubow, S. H., et al. 1996, ApJ, 470, 1187
Rauer, H., Aerts, C., Cabrera, J., et al. 2025, ExA, 59, 26
Reinhold, T., Bell, K. J., Kuszlewicz, J., Hekker, S., & Shapiro, A. I. 2019, A&A, 621, A21
Ricker, G. R., Winn, J. N., Vanderspek, R., et al. 2014, SPIE, 9143, 914320
Robrade, J., Stelzer, B., & Schmitt, J. H. M. M. 2023, A&A, 669, A155
Rogers, F. J., & Nayfonov, A. 2002, ApJ, 576, 1064
Romaniello, M., Primas, F., Mottini, M., et al. 2008, A&A, 488, 731
Royer, P., Merle, T., Dsilva, K., et al. 2024, A&A, 681, A107
Santos, A. R. G., Metcalfe, T. S., Kochukhov, O., et al. 2025, A&A, 698, L23
Scargle, J. D. 1982, ApJ, 263, 835
Scuflaire, R., Théado, S., Montalbán, J., et al. 2008, Ap&SS, 316, 83
Skrutskie, M. F., Cutri, R. M., Stiening, R., et al. 2006, AJ, 131, 1163
Soubiran, C., & Girard, P. 2005, A&A, 438, 139
TESS Team 2021a, TESS "Fast" Light Curves - All Sectors STScI/MAST, doi:10.17909/T9-ST5G-3177
TESS Team 2021b, TESS Light Curves - All Sectors, STScI/MAST, doi:10.17909/T9-NMC8-F686
Thoul, A. A., Bahcall, J. N., & Loeb, A. 1994, ApJ, 421, 828
Tokovinin, A., Mason, B. D., & Hartkopf, W. I. 2010, AJ, 139, 743
Tokovinin, A., Mason, B. D., Hartkopf, W. I., Mendez, R. A., & Horch, E. P. 2015, AJ, 150, 50
Tokovinin, A., Mason, B. D., Mendez, R. A., Costa, E., & Horch, E. P. 2020, AJ, 160, 7
van Leeuwen, F. 2007, A&A, 474, 653
van Saders, J. L., Ceillier, T., Metcalfe, T. S., et al. 2016, Natur, 529, 181
Vaughan, A. H., Preston, G. W., & Wilson, O. C. 1978, PASP, 90, 267
Vernazza, J. E., Avrett, E. H., & Loeser, R. 1981, ApJS, 45, 635
Vieira, K., Carraro, G., Korchagin, V., et al. 2022, ApJ, 932, 28
Villaver, E., & Livio, M. 2009, ApJL, 705, L81
Wilson, O. C. 1968, ApJ, 153, 221
Wilson, O. C. 1978, ApJ, 226, 379